Deformation mechanisms of idealised cermets under multi-axial loading

E. Bele[1], A. Goel[1], E. G. Pickering[1], G. Borstnar[2], O. L. Katsamenis[3], F. Pierron[2], K. Danas[4] and V. S. Deshpande[1*]

[1]Department of Engineering, University of Cambridge, Trumpington Street, Cambridge, UK.
[2] University of Southampton, Faculty of Engineering and the Environment, SO17 1BJ Southampton, UK.
[3] University of Southampton, μ-VIS X-Ray Imaging Centre, Faculty of Engineering and the Environment, SO17 1BJ Southampton, UK.
[4]LMS, Ecole Polytechnique, CNRS, Université Paris-Saclay, 91128 Palaiseau, France.

Abstract

The response of idealised cermets comprising approximately 60% by volume steel spheres in a Sn/Pb solder matrix is investigated under a range of axisymmetric compressive stress states. Digital volume correlation (DVC) analysis of X-ray micro-computed tomography scans (μ-CT), and the measured macroscopic stress-strain curves of the specimens revealed two deformation mechanisms. At low triaxialities the deformation is granular in nature, with dilation occurring within shear bands. Under higher imposed hydrostatic pressures, the deformation mechanism transitions to a more homogeneous incompressible mode. However, DVC analyses revealed that under all triaxialities there are regions with local dilatory and compaction responses, with the magnitude of dilation and the number of zones wherein dilation occurs decreasing with increasing triaxiality. Two numerical models are presented in order to clarify these mechanisms: (i) a periodic unit cell model comprising nearly rigid spherical particles in a porous metal matrix and (ii) a discrete element model comprising a large random aggregate of spheres connected by non-linear normal and tangential "springs". The periodic unit cell model captured the measured stress-strain response with reasonable accuracy but under-predicted the observed dilation at the lower triaxialities, because the kinematic constraints imposed by the skeleton of rigid particles were not accurately accounted for in this model. By contrast, the discrete element model captured the kinematics and predicted both the overall levels of dilation and the simultaneous presence of both local compaction and dilatory regions with the specimens. However, the levels of dilation in this model are dependent on the assumed contact law between the spheres. Moreover, since the matrix is not explicitly included in the analysis, this model cannot be used to predict the stress-strain responses. These analyses have revealed that the complete constitutive response of cermets depends both on the kinematic constraints imposed by the particle aggregate skeleton, and the constraints imposed by the metal matrix filling the interstitial spaces in that skeleton.

Keywords: cermets, porous plasticity, kinematic constraints, discrete element, digital volume correlation, micro-computed tomography.

* Corresponding author. E-mail address: vsd@eng.cam.ac.uk

1. Introduction

Cermets are particulate composites comprising a high volume fraction of ceramic particles (typically carbides, nitrides, and oxides, in the range of 50-95% by volume) within a ductile metal binder phase (e.g. Mo, Ni, Co, Al) (ASTM Committee C-21, 1955; Tinklepaugh and Crandall, 1960). They offer a good compromise between the hardness of ceramics and toughness of metals, e.g. typical values for WC/Co composites are in the range of 500-2000 HV and 8-20 MPa $m^{1/2}$, respectively (Fang, 2005). This combination of mechanical properties has led to their extensive use in small volume applications such as tips of cutting tools. Recent advances in manufacturing methods have provided the ability to produce cermets in large volumes at low cost. This has resulted in cermets being considered as materials for lightweight ballistic armour applications, where the high hardness is required to erode the projectile (Shockey et al., 1990; Walley, 2010), and the improved toughness increases the ability of the armour to sustain multiple impacts (Blumenthal et al., 1994; Compton and Zok, 2013).

The prediction of the strength of cermets has received considerable attention. Current models typically fall into two categories: (i) empirical e.g. the models for hardness by Lee and Gurland (1978) and Engqvist et al. (2002), and (ii) microstructurally motivated models based on either homogenisation schemes (Arsenault and Taya, 1987; Bao et al., 1991; Christman et al., 1989) or dislocation models (Gustafson et al., 1997; Lee et al., 1998; Taya et al., 1991). The predictive microstructurally motivated models are primarily based on extending approaches developed for composites such as the so-called self-consistent models (Budiansky, 1965; Hershey, 1954; Hill, 1965) and models that provide bounds on the response of particulate composites (Hashin and Shtrikman, 1962). These models have the advantage that they do not make *a priori* assumptions on the microstructure but rather describe the microstructure through statistical information such as volume fraction and particle position correlation functions. However, this statistical information is typically only valid in the low particle volume fraction limit (< 20% by volume particles) when particle-particle contacts are negligible. By contrast, most commercial cermets with ~80% particle volume fractions are well above the percolation threshold and a large number of the ceramic particles in these cermets are parts of percolated chains of ceramic particles.

The percolated chains, known as *force chains* in the granular materials literature (Liu et al., 1995; Travers et al., 1987) have a very significant effect on the properties of the cermets. In fact, cermets with high volume fractions of hard ceramic inclusions are more akin to a granular medium with a high cohesive strength rather than a typical particle-reinforced composite. For example, recent studies (Pickering et al., 2016; Tarantino et al., 2016) have demonstrated that the multi-axial yield response of cermets is not solely governed by the von-Mises stress. Rather, similar to granular materials, cermets dilate under compression and thus their strength is also dependent on the imposed hydrostatic pressure. Moreover, Bele and Deshpande (2015) have demonstrated that composite models based on periodic unit cells significantly under-predict the strength of cermets as they do not include the effects of force chains. Similar effects are also observed in other high volume particulate composites such as asphalt (Deshpande and Cebon, 1999) and polymer-bonded explosives (Bardenhagen and Brackbill, 1998). Discrete element models (Cundall and Strack, 1979), wherein the particles are modelled as discrete bodies interacting via contact relations are likely to be more appropriate for modelling the deformation of cermets. These approaches have been successfully used to predict the yielding and dilation of soils during confined

compression (McDowell and Harireche, 2002; Powrie et al., 2005) as well as the uniaxial deformation of asphalt (Cai et al., 2013; Collop et al., 2007; Wu et al., 2011). However, there have been no reported attempts of discrete element models for cermets.

The experimental characterisation of the deformation of cermets has primarily been based on macroscopic strain measurements. While such measurements give some information on the deformation, they provide little insight into the microscopic deformation processes including the particle kinematics. By contrast, digital image correlation (DIC) techniques have been extensively deployed to quantify the deformation of soils. For example DIC techniques to observe deformation mechanisms in two-dimensional (2D) uniaxial compression (Desrues et al., 1996, 1985; Finno et al., 1997) have demonstrated the existence of force chains under plane strain loading in granular materials. Moreover, with the increased spatial resolution of X-ray micro-tomographic techniques, it has now become possible to quantify the three-dimensional (3D) deformation of granular materials using the so-called digital volume correlation (DVC) technique. Using this technique, Lenoir et al. (2007) have reported full-field incremental strain measurements during confined compression of argillaceous rock and Hu et al. (2015) studied deformation mechanisms in uniaxially compressed polymer bonded sugar (PBS) specimens. Such DVC measurements are typically not reported for triaxial compression due to the complexity of taking X-ray scans of specimens within high-pressure triaxial cells.

1.1 Scope of this study

Commercial cermets typically have very high yield strengths (in the range 5-10 GPa), which makes testing of these materials difficult. Thus, most strength measurements rely on hardness measurements that are typically difficult to interpret. The aim of this study is to develop an understanding of the deformation mechanisms of cermets under multi-axial loading. We therefore use the so-called *idealised cermets* developed by Bele and Deshpande (2015). These materials comprise hard steel spheres in soft metal matrix and have a significantly lower yield strength compared to commercial cermets. However, a similar contrast in the properties of the phases of the idealised and commercial cermets makes the idealised cermets suitable model materials to study the deformation mechanisms in commercial cermets.

The outline of the paper is as follows. Firstly, to clarify the deformation mechanisms under a range of stress triaxialities, μ-CT imaging was combined with *ex-situ* triaxial compression tests and the results were analysed by means of DVC. Next, two modelling approaches are reported in an attempt to gain insight into these measurements: (i) a periodic unit cell model comprising nearly rigid spheres in a porous plastic matrix and (ii) a discrete element model comprising a large number of randomly packed spheres interacting via a contact law. The features and drawbacks of these models are discussed and used to reveal the key deformation mechanisms that govern the mechanical response of the idealised cermets.

2. Experimental protocol

The overall aim of the experimental program is to determine the deformation modes of the idealised cermets as a function of stress triaxiality. To achieve this aim, we

conducted axisymmetric triaxial compression tests, interrupted at known macroscopic strains $\bar{E}_e$ to acquire X-ray micro-computed tomograms (μ-CT). The resulting μ-CT volumes derived after each loading step were then used to perform a DVC analyses to reveal the deformation modes. Here we briefly describe the main aspects of the experimental methods.

2.1 Manufacture of specimens

Idealised cermets comprising a volume fraction $V_f \approx 0.60$ of 2 mm diameter AISI 52100 steel spheres (referred to subsequently as *particles*) in a Sn/Pb solder matrix (Sn 60, Pb 38, Ag 2 wt.%), were investigated in this study. The cermet specimens were circular cylinders of diameter 18.5 mm and height 40 mm and were manufactured using the procedure described in Bele and Deshpande (2015) and Pickering et al. (2016). Briefly, the steel spheres were cleaned via ultrasonic vibration in an acetone bath and then packed into a cylindrical crucible of the diameter ~18.5 mm. The crucible was vibrated under a low applied axial compressive stress of ≈ 0.1 MPa to maximise the packing density. High temperature magnets were then placed around the periphery of the crucible to preserve the skeleton structure of the steel spheres, and solder powder (of average particle size 25-38 μm) was infiltrated into the interstitial sites between the particles. A small amount of ZnCl flux was added to improve interfacial adhesion, and the assembly was pressure-cast at a temperature of 200°C for 1 hr. An optical image of the as-cast specimen is included in Fig. 1a, and a X-ray computed tomogram through the centre of the specimen along the longitudinal axis is shown in Fig. 1b. μ-CT imaging revealed that the void volume fraction was in the range 1.5% to 5%. The Young's modulus and yield strength of the AISI 52100 steel was 210 GPa and 2.1 GPa, respectively while the Sn/Pb solder had modulus and yield strength values of 32 GPa and ~30-40 MPa, respectively.

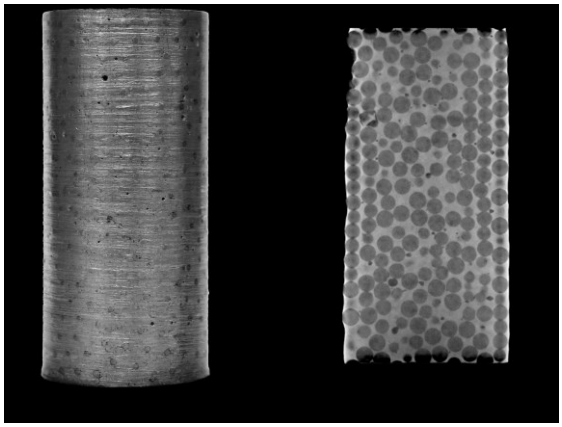

Figure 1: (a) Photograph of the as-cast idealised cermet specimen and (b) a computed tomogram through the centre of the specimen along the longitudinal axis.

2.2 Interrupted triaxial tests

A high-pressure apparatus (see Pickering et al. (2016) for details of the triaxial cell) was used to subject the specimens to axisymmetric triaxial compression tests (Fig. 2a). It consists of a pressure cell with a maximum capacity of 100 MPa, and a piston for the application of axial force. Hydraulic fluid was used as the pressurising medium, and axial load is applied by displacing the piston via a screw-driven test machine. A submerged load cell provided readings of the axial load independent of the pressure of the surrounding fluid. Two linear variable differential transformer (LVDT) transducers were attached to the specimen in order to measure the axial displacement imposed on

the specimen. A third LVDT was attached to the mid-height of the specimen to measure the change in specimen diameter over a 3 mm central portion of the cylindrical specimen.

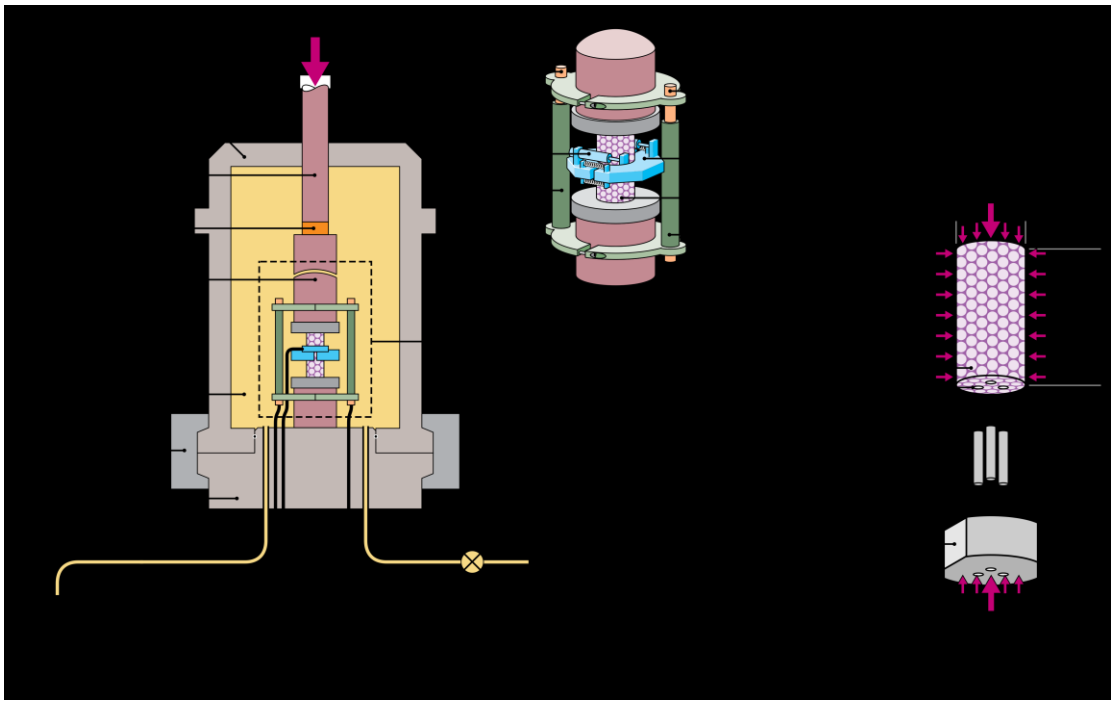

Figure 2: (a) Sketch of the triaxial apparatus used to apply the axisymmetric stress states. The inset shows a magnified view of the specimen with the axial and radial LVDTs used to measure strain. (b) Sketch of the axisymmetric stress state and the three-pin localisation system used to ensure specimen alignment between successive CT scans.

The applied stresses/forces on a cylindrical specimen of initial height ℓ_0 and radius R_0 are sketched in Fig. 2b. The hydraulic fluid exerts a pressure P (taken to be positive in compression) on the specimen and the axial force measured by the submerged load cell is F_a (this is a force in excess of that exerted by the fluid pressure, and is taken to be positive in compression). The radial Cauchy stress is $-P$, and the axial stress can be inferred from F_a as follows. The current specimen height ℓ and radius R give the axial and radial stretches as $\lambda_a = \ell/\ell_0$ and $\lambda_r = R/R_0$, respectively. The nominal axial and radial stresses then follow as $\bar{N}_a = -[F_a/(\pi R_0^2) + P\lambda_r^2]$ and $\bar{N}_r = -P\lambda_a\lambda_r$, respectively. We can then define a nominal mean stress as

$$\bar{N}_m \equiv \frac{\bar{N}_{kk}}{3} = \frac{2}{3}\bar{N}_r + \frac{\bar{N}_a}{3}, \tag{2.1}$$

where $\bar{N}_{ij}$ denotes the nominal stress tensor. Similarly, an invariant of the trace-less nominal stress (analogous to the von-Mises stress) is given by

$$\bar{N}_e \equiv \sqrt{\frac{3}{2}\bar{N}'_{ij}\bar{N}'_{ij}} = |\bar{N}_a - \bar{N}_r|, \tag{2.2}$$

where $\bar{N}'_{ij} = \bar{N}_{ij} - \bar{N}_m\delta_{ij}$, with δ_{ij} denoting the Kronecker delta.

Tests were conducted along proportional stress paths with the direction of the stress path defined by the relation $\bar{N}_m = -\eta\bar{N}_e$. The triaxiality parameter η can take values

over the range $\eta = 1/3$ (uniaxial compression) to $\eta = \infty$ (hydrostatic compression). In the proportional loading tests of this study, η was kept constant throughout the experiments by a feedback process whereby the fluid pressure P and the axial stress $\bar{N}_a$ were increased while keeping the triaxiality η fixed.

In the remainder of this study we discuss distributions of the Green-Lagrange strains as measured by the DVC analysis, and thus here we express the measured macroscopic strains in terms of the Green-Lagrange strains. The radial and axial Green-Lagrange strains follow from the stretches via the relations

$$\bar{E}_r = \frac{1}{2}(\lambda_r^2 - 1), \tag{2.3}$$

and

$$\bar{E}_a = \frac{1}{2}(\lambda_a^2 - 1), \tag{2.4}$$

respectively. Then with $\bar{E}_{ij}$ denoting the Green-Lagrange strain tensor, we define a mean strain given by $\bar{E}_m \equiv \bar{E}_{kk}$, a trace-less strain tensor $\bar{E}'_{ij} = \bar{E}_{ij} - \delta_{ij}\bar{E}_m/3$ and an invariant of this trace-less strain, $\bar{E}_e \equiv \sqrt{(2/3)\bar{E}'_{ij}\bar{E}'_{ij}}$, analogous to the von-Mises effective strain. For axisymmetric loading these reduce to

$$\bar{E}_m = 2\bar{E}_r + \bar{E}_a, \tag{2.4}$$

and

$$\bar{E}_e = \frac{2}{3}|\bar{E}_r - \bar{E}_a|. \tag{2.6}$$

We emphasise that in general $\bar{E}_m$ is not equal to the volumetric strain, i.e. $\bar{E}_m \neq \Delta V/V_0$, where ΔV and V_0 are the change in volume and original volume respectively. Thus, $\bar{E}'_{ij}$ is not a deviatoric strain in the sense of representing a deviation from the volumetric strain. However, as discussed in Appendix A, for the relatively small strains considered in this study $\bar{E}_m \approx \Delta V/V_0$ and it suffices to use the strain measures $\bar{E}_m$ and $\bar{E}_e$ to illustrate volumetric and shear deformations. Given that we present results in terms of the Green-Lagrange strains, it is appropriate to use the 2nd Piola-Kirchhoff stress measure. The work-conjugate 2nd Piola-Kirchhoff stresses to $\bar{E}_a$ and $\bar{E}_r$ are $\bar{S}_a = \bar{N}_a/\lambda_a$ and $\bar{S}_r = \bar{N}_r/\lambda_r$, respectively. Then, analogous to Eqs. (2.1) and (2.2), we define the mean and effective stress as $\bar{S}_m \equiv \bar{S}_{kk}/3$ and $\bar{S}_e \equiv \sqrt{(3/2)\bar{S}'_{ij}\bar{S}'_{ij}}$, respectively where $\bar{S}_{ij}$ is the 2nd Piola-Kirchhoff stress tensor and $\bar{S}'_{ij} = \bar{S}_{ij} - \bar{S}_m\delta_{ij}$ the corresponding trace-less stress.

All experiments reported here were conducted for an applied loading rate $\dot{\bar{N}}_e \approx 10$ kPa s^{-1} and prior to the start of each test the specimen was consolidated within the triaxial cell by applying a pure hydrostatic pressure $P = 100$ MPa. This consolidation step was found to improve the repeatability of the measurements. The DVC analysis was conducted using three specimens loaded along proportional stress paths of $\eta = 1/3, 0.75$ and 1.0. The images for the DVC were acquired via X-ray micro-tomography

(μ-CT) at four strain levels: an initial reference state scan at $\bar{E}_e = 0$ (representing the state of the specimen after consolidation to $P = 100$ MPa), and three scans acquired by interrupting the triaxial test and unloading to accumulated strain levels $\bar{E}_e = 0.02, 0.035$ and 0.055. After each scan, the specimen was reinserted into the triaxial cell and loaded to the next strain level. Since the DVC analysis requires fixed reference points, the specimens were attached to a small, non-symmetric platen via three tool steel pins; see Fig. 2b. This enabled us to maintain the orientation of the specimen between each μ-CT scan and loading within the triaxial cell.

2.3 X-ray micro-computed tomography and digital volume correlation

The μ-CT scans for the DVC analyses were acquired using a custom Nikon/Metris scanner consisting of a 450 kVp power source coupled with a cesium-iodide detector (1621 Perkinelmer). The specimens were positioned 116.5 mm from the source, resulting in a pixel resolution of 28.3μm. Each tomogram comprised 1601 angular projections collected at an angular step of $\sim 0.225^{o}$ over a 360^{o} rotation of the sample. The projection data was were reconstructed using Nikon's CTPro and CTAgent reconstruction software, which uses a filtered back projection algorithm.

Similar to digital image correlation, DVC involves dividing the 3D scan volume into smaller sub-volumes, which can then be tracked between load steps using the internal microstructure of the material (Bay et al., 1999). The new position of the sub-volume centroid is taken to be at a location where the correlation coefficient between the original and displaced sub-volume is best. Here we performed the DVC analysis using DaVis software (LaVision, DaVis v.8.2.3 Software, Goettingen, Germany) by comparing the three strained states back to the reference scan at $\bar{E}_e = 0$. The strain fields are then determined from the spatial gradients of displacement vector fields of the sub-volumes over a gauge length equal to 50% of the sub-volume size, as described in Gillard et al. (2014). A noise study was performed using sub-volume sizes between 24 to 192 voxels (based on the resolution of the μ-CT scan each voxel represents a cube of side length ~ 28.3 μm) (Gillard et al., 2014). A 150 voxel sub-volume size with 50% overlap gave the best compromise between noise and an adequate spatial resolution for strain in these specimens. Thus, the DVC was performed with cubes of side ~ 4.2 mm (volume ~ 64 mm^3): with the 50% overlap this implied that approximately 7 sub-volume cubes were present in the analysis across the diameter of the specimens.

3. Summary of experimental results

We proceed to describe the key findings of the experimental study on the triaxial responses of idealised cermets, and the associated deformation modes/strain distributions as determined from the DVC analysis.

3.1 Mechanical responses

A detailed study of the triaxial response of the idealised cermets is presented in Pickering et al. (2016). Here we summarise some key findings in order to explain the context of the DVC strain distribution measurements. The measured equivalent stress versus strain responses ($\bar{S}_e - \bar{E}_e$) responses for triaxiality values in the range $\eta = 1/3$ (uniaxial compression) to $\eta = 1.5$ are plotted in Fig. 3a, and the corresponding variations of the mean strain $\bar{E}_m$ with the effective strain $\bar{E}_e$ are included in Fig. 3b. The stress-strain curves of Fig. 3a show that both the initial elastic response and the yield stress (defined at the 0.2% strain offset) are largely independent of η. However,

the subsequent plastic hardening response is strongly affected by the triaxiality: while the uniaxial response is approximately perfectly plastic, the plastic hardening rate increases up to $\eta = 1$. Intriguingly, the $\bar{S}_e - \bar{E}_e$ curves become virtually identical for $\eta \geq 1$. Some insight into this triaxiality dependent response is given by the corresponding $\bar{E}_m - \bar{E}_e$ curves included in Fig. 3b. In the low triaxiality limit ($1/3 \leq \eta \leq 0.75$), two distinct regimes are seen: (i) an initial compaction regime where $d\bar{E}_m/d\bar{E}_e < 0$, and (ii) a dilation regime with $d\bar{E}_m/\, d\bar{E}_e > 0$, wherein the volume of the specimen increases even though the hydrostatic pressure is compressive. While dilation commences very early under uniaxial compression (at approximately the yield strain of $\bar{E}_e = 0.5\%$), the dilatory regime is delayed at higher triaxialities, e.g. starting at $\bar{E}_e = 3.5\%$ in the tests with $\eta = 0.75$. We argue that similar to granular media, the work done against the hydrostatic pressure by the dilatory response of the cermet results in the plastic hardening rate increasing with η, as seen in Fig. 3a. With further increases in triaxiality, the dilatory part of the response is further delayed: over the strain levels tested here no dilation occurred in the regime $\eta \geq 1$, and the $\bar{E}_m - \bar{E}_e$ curves are very similar (Fig. 3b). Since the plastic response is now nearly volumetrically incompressible, the stress-strain curves are uniquely described by the effective stress $\bar{S}_e$ with no sensitivity to η as seen in Fig. 3a.

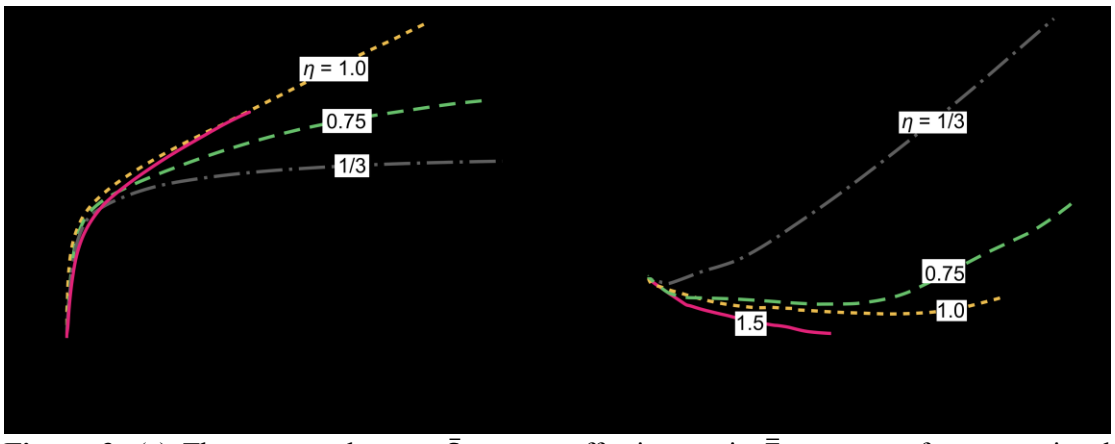

Figure 3: (a) The measured stress $\bar{S}_e$ versus effective strain $\bar{E}_e$ response for proportional loading of the idealised cermet specimens at selected values of the triaxiality η; (b) the volumetric strain $\bar{E}_m$ versus $\bar{E}_e$ responses corresponding to the curves in (a).

The initial yield surface of these idealised cermets and the evolution of this surface with plastic strain is summarised in Fig. 4. The initial yield strength is obtained by the 0.2% strain offset in the $\bar{S}_e - \bar{E}_e$ curves. A plot of the stress pair $(\bar{S}_m, \bar{S}_e)$ corresponding to this definition of the yield point at all the values of η tested here marks the locus of the initial yield surface. Loci of $(\bar{S}_m, \bar{S}_e)$ at three selected values of applied effective strain $\bar{E}_e$, and fits to the data using the yield criterion suggested in Pickering et al. (2016) are also included. Superimposed on these loci is the direction of the plastic strain rate vector $(\dot{\bar{E}}_m, \dot{\bar{E}}_e)$ at selected loading points, with the $\dot{\bar{E}}_m$ and $\dot{\bar{E}}_e$ axes co-incident with the $\bar{S}_m$ and $\bar{S}_e$ axes respectively. These measurements suggest that two distinct deformation mechanisms/regimes exist:
(i) At low triaxialities, the yield surface has a Drucker and Prager (1952) characteristic with the yield strength being pressure dependent and the response dilatant even under compressive hydrostatic stresses, similar to granular materials.

(ii) At high triaxialities, the yield surface asymptotes to a von-Mises surface with the yield strength independent of pressure and the overall deformation nearly incompressible.

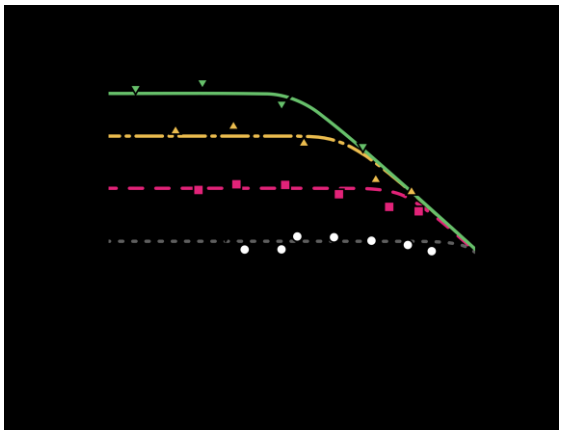

Figure 4: The measured yield surfaces of the idealised cermets. The initial yield surface and the evolution of the surface for 3 additional values of the effective strain $\bar{E}_e$ are included. The plastic strain rate vectors are included for selected loading points with the $\dot{\bar{E}}_e$ and $\dot{\bar{E}}_m$ axes co-incident with the $\bar{S}_e$ and $\bar{S}_m$ axes, respectively.

3.2 Strain distributions

While the strain measurements in Fig. 3b give the overall deformation state, it is unlikely that a "granular" medium like this idealised cermet will undergo homogenous deformation. We therefore report DVC measurements of the strain distribution. The Green-Lagrange strain tensor is denoted as E_{ij} and, analogous to definitions used for the macroscopic average strains in Section 2, we define a mean strain as $E_m = E_{kk}$ and a trace-less strain $E'_{ij} = E_{ij} - \delta_{ij}E_{kk}/3$, where δ_{ij} is the Kronecker delta. The effective strain is then defined as

$$E_e = \sqrt{\frac{2}{3}E'_{ij}E'_{ij}}. \qquad (3.1)$$

Distributions of E_m and E_e on a longitudinal cross-section through the specimen are included in Figs. 5 and 6 respectively for three proportional stressing paths ($\eta = 1/3$, 0.75 and 1.0) at applied macroscopic strains $\bar{E}_e = 0.02$, 0.035 and 0.055. First consider the uniaxial compression ($\eta = 1/3$) case. Early in the deformation ($\bar{E}_e = 0.02$), the strain distributions are reasonably uniform though it is clear that nearly the entire specimen is undergoing dilation (Fig. 5a). With increasing $\bar{E}_e$, the deformation becomes more localised and both the E_m and E_e distributions show an inclined band near the top of the specimen within which the strains significantly exceed those in the remainder of the specimen. To illustrate that this band exists through the specimen we include in Fig. 7 contours of E_m for $\bar{E}_e = 0.055$ on four longitudinal cross-sections through the specimen at orientations φ: this orientation is defined in the inset of Fig. 7 ($\varphi = 0^o$ is an arbitrarily chosen section through the specimen). The band of localised deformation is seen on all orientations confirming that this band persists through the specimen. With increasing triaxiality (i.e. $\eta = 0.75$ and 1.0) two main changes occur: (i) the deformation is seen to become more homogenous and (ii) the level of dilation decreases. Regions of both compaction and dilation are seen at $\bar{E}_e = 0.055$ in the

specimens loaded with $\eta = 0.75$ and 1.0, however the values of positive E_m remain small in relation to the $\eta = 1/3$ case.

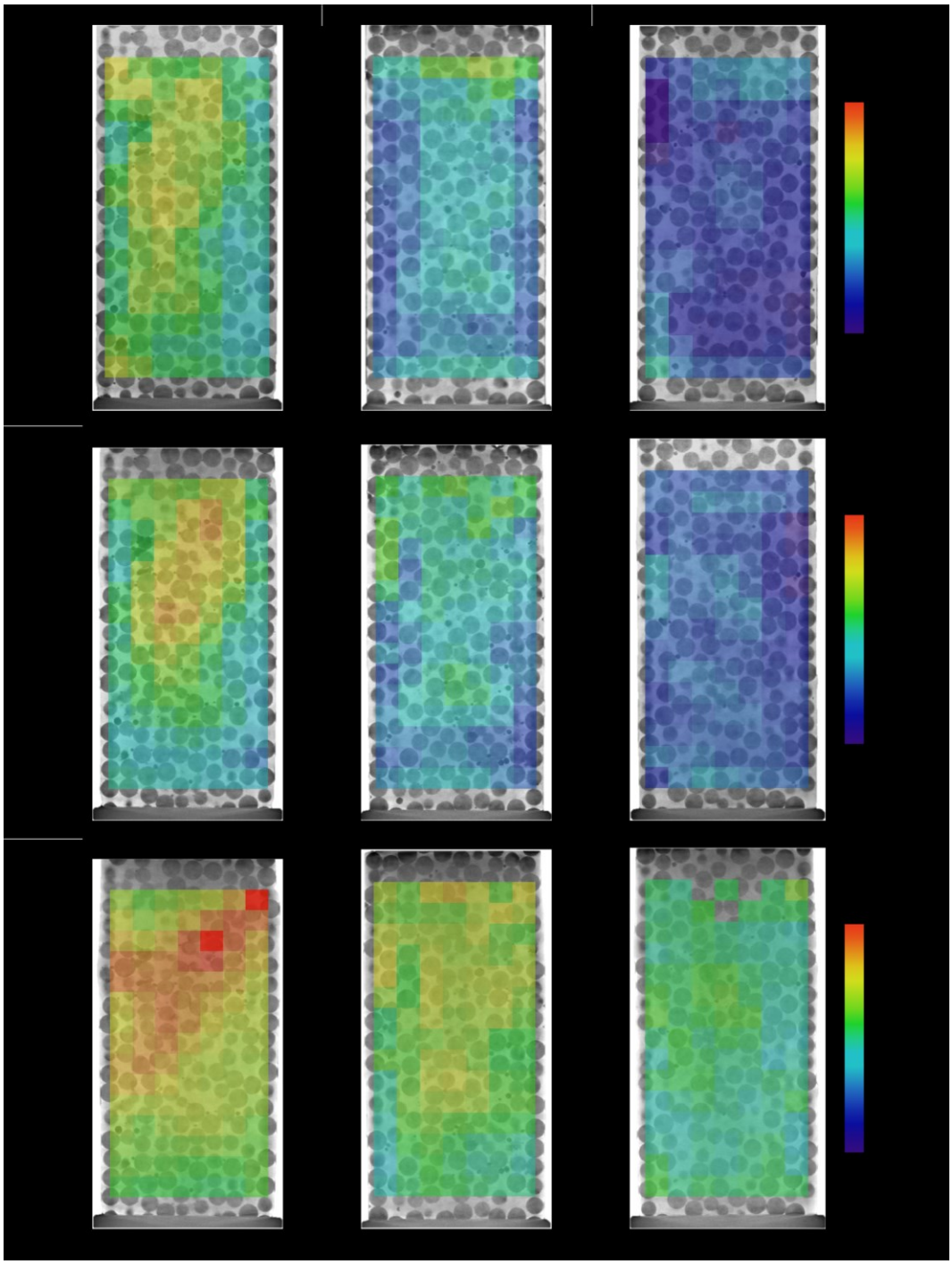

Figure 5: Digital volume correlation (DVC) measurements of the spatial distribution of the volumetric strain E_m on a longitudinal section of the idealised cermet specimen at three applied macroscopic strains $\bar{E}_e$. Results are shown for three stress paths (a) $\eta = 1/3$, (b) $\eta = 0.75$ and (c) $\eta = 1.0$.

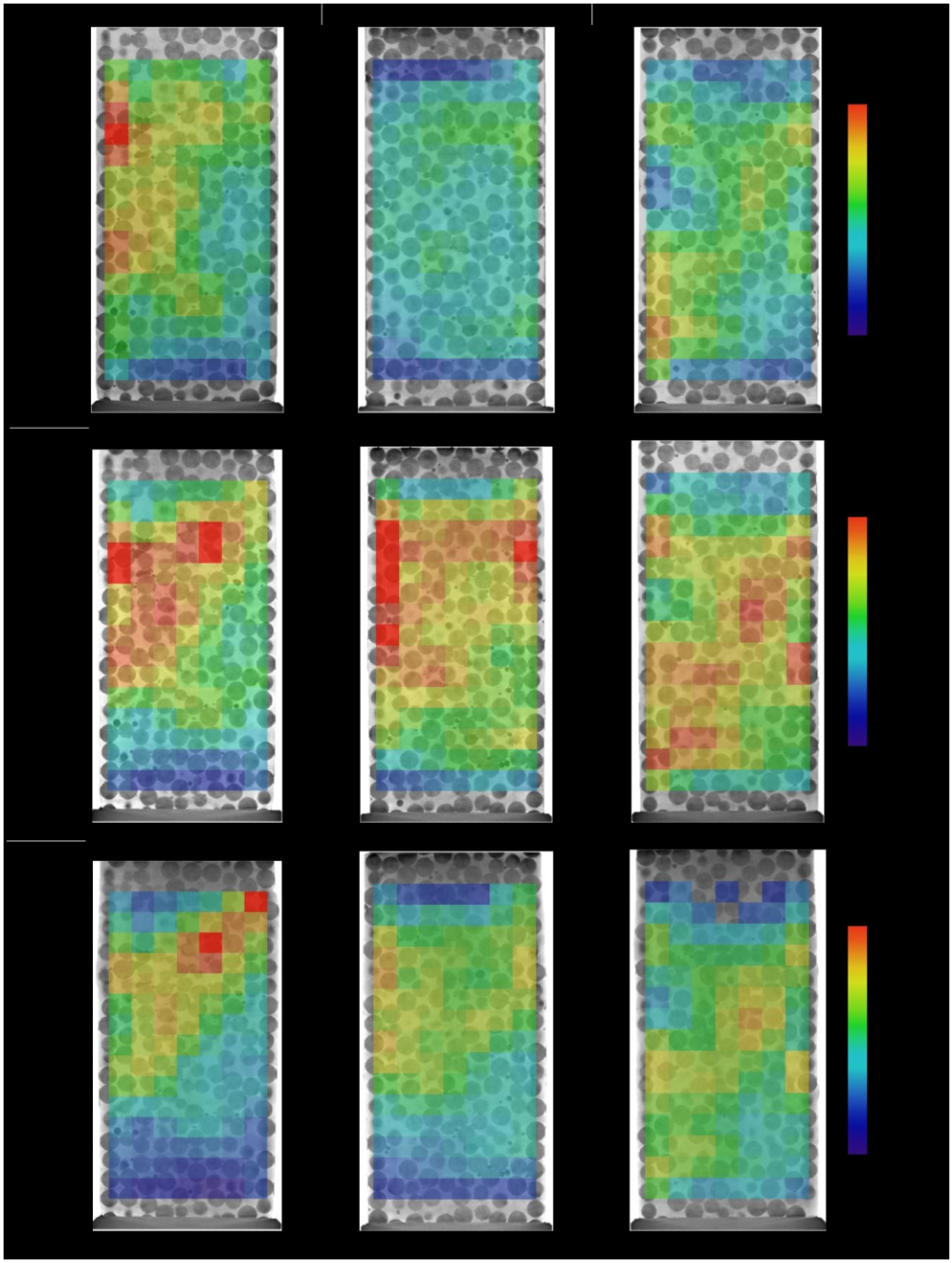

Figure 6: Digital volume correlation (DVC) measurements of the spatial distribution of the effective strain E_e on a longitudinal section of the idealised cermet specimen at three applied macroscopic strains $\bar{E}_m$. Results are shown for three stress paths (a) $\eta = 1/3$, (b) $\eta = 0.75$ and (c) $\eta = 1.0$.

To further emphasise these differences, we define an average volumetric strain $\hat{E}_m(z)$ as the average value of E_m on the plane $x_3 = z$ where the co-ordinate system x_i is defined in the inset in Fig. 7 and $x_3 = 0$ is the bottom face of the cylindrical specimen. The variations of $\hat{E}_m$ with the normalised co-ordinate z/ℓ_0, where $\ell_0 = 40$ mm is the initial height of specimen, are included in Figs. 8a, 8b and 8c for $\eta = 1/3$, 0.75 and 1.0, respectively. In each case, we include the variations at $\bar{E}_e = 0.02$, 0.035 and 0.055. The overall conclusions from the distributions in Fig. 5 are further confirmed here, viz.:

(i) the level of volumetric straining decreases with increasing η and (ii) the deformation is more localised at the lower values of η (a band with high deformation for the specimen loaded with $\eta = 1/3$ is marked and labelled as a "localised band" in Fig. 8a).

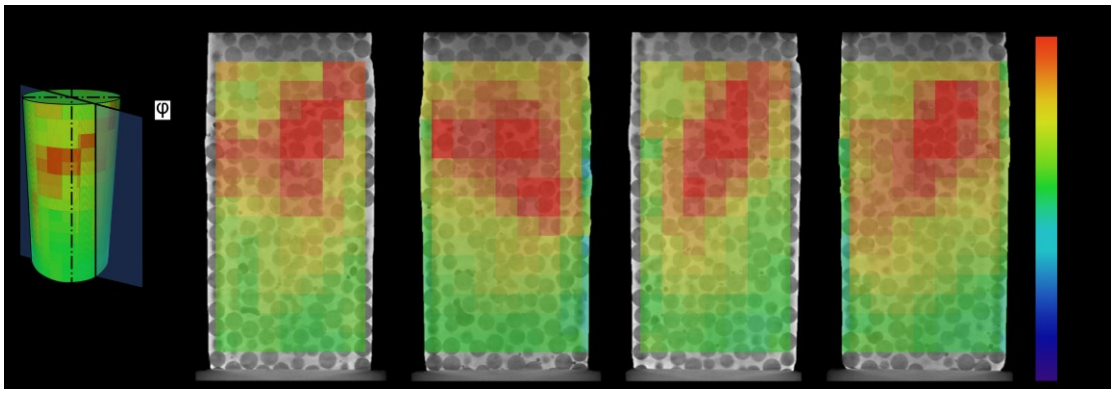

Figure 7: Digital volume correlation (DVC) measurements of the spatial distribution of the volumetric strain E_m on four longitudinal sections through the idealised cermet specimen subjected to a macroscopic strain $\bar{E}_e = 0.055$ under uniaxial compression ($\eta = 1/3$). The orientation φ of the sections is defined in the inset on a 3D plot of the E_m distributions from the DVC analysis along with the co-ordinate system used to describe the specimen.

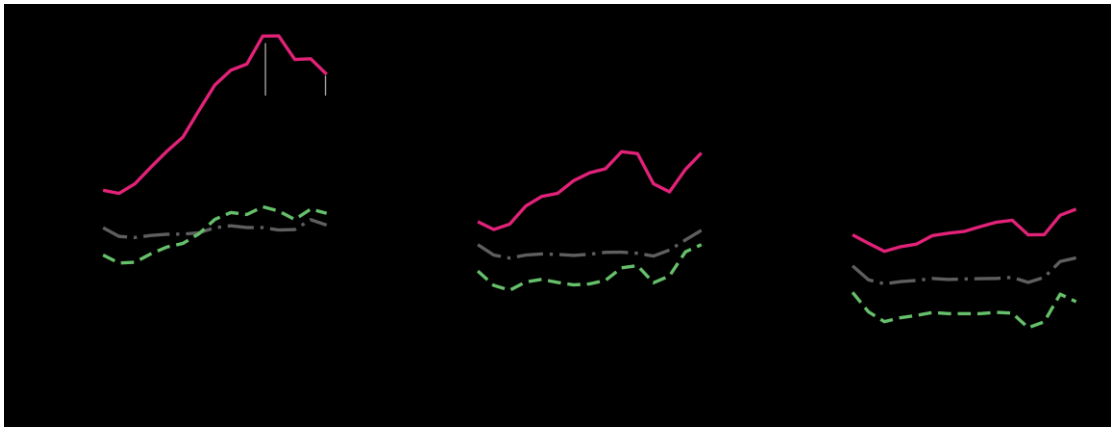

Figure 8: Digital volume correlation (DVC) measurements of the average volumetric strain $\hat{E}_m$ as a function of the normalised axial co-ordinate z/ℓ_0. Measurements are shown for the specimen deformed under stress paths (a) $\eta = 1/3$, (b) $\eta = 0.75$ and (c) $\eta = 1.0$ for overall strain levels $\bar{E}_e = 0.02$, 0.035 and 0.055 in each case.

These measurements confirm our qualitative understanding that a transition in the deformation mechanism from granular (dilatory response within a shear band) to metal-like (uniform, incompressible deformation) occurs with increasing stress triaxiality. Importantly, they show that deformation is heterogeneous with local dilatory and compaction regions. The magnitude of dilation and the number of dilating zones decreases with increasing η, giving rise to the observed changes in the macroscopic strain states. However, several aspects remain unclear. These include: (i) the microscopic mechanisms by which the transition from dilatory to incompressible behaviour occurs; and (ii) the roles of the matrix and the particle skeleton in dictating the kinematic response of the cermets. We proceed to develop two types of numerical models in an attempt to address these questions.

4. Analysis of periodic particulate composites

Here we model the idealised cermet as a periodic composite comprising spherical elastic particles in a voided elastic-plastic matrix. Such periodic models have been used extensively to analyse metal matrix composites (MMCs) following the initial work of Bao et al. (1991). Cermets differ from MMCs by the fact that they comprise a significantly higher volume fraction of particles/inclusions compared to MMCs, and here we aim to investigate whether such a model is capable of capturing their response.

4.1 Brief description of model

We consider a three-dimensional unit cell with the spherical particles arranged in a face-centred-cubic (FCC) lattice as shown in Fig. 9. This is done in order to be able to reach higher local strains in the matrix while minimising mesh distortion. The particles are assumed to be isotropic elastic with shear modulus G_p and Poisson's ratio ν_p while the matrix is modelled as a porous elastic-plastic solid. The porous solid is modelled using a simplified version of the modified variational model (MVAR) presented in Danas and Aravas (2012) based on the nonlinear homogenisation approach of Ponte Castañeda (1991). Thus, unlike the particles, the voids (shown in the inset of Fig. 9) are not discretely modelled but rather smeared-out in the matrix. This approximation is acceptable given the large separation of length scales between the particle and void sizes. The general MVAR model considers a single family of ellipsoidal voids with arbitrary orientation, leading to an overall anisotropic response. Our aim here is to qualitatively investigate the fidelity of such a modelling approach for analysing cermets and thus we consider a simplified version wherein we restrict attention to spherical voids whose shape remains unchanged with deformation[†] The resulting model thus remains isotropic at finite strains and reduces to the Gurson (1977) model in the hydrostatic loading limit but is more compliant for non-zero deviatoric stresses. For the sake of completeness we briefly describe the key constitutive equations of the matrix phase.

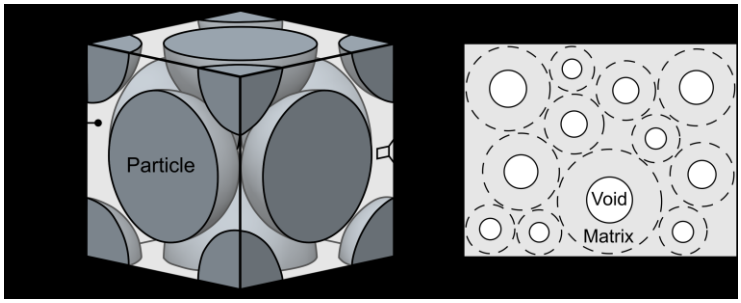

Figure 9: Sketch of the 3D periodic unit cell comprising nearly rigid spherical particles in a face-centred-cubic arrangement with the interstitial spaces filled with a porous plastic matrix. The inset shows the microstructure of the homogenised porous matrix. The co-ordinate system used to describe the stress-state is also indicated.

The matrix is modelled as an isotropic elastic plastic solid with shear modulus G_m and Poisson's ratio ν_m. The elastic properties are assumed to be fixed and do not change with evolving porosity f. The plastic response is described by a yield surface given in

[†] At high triaxialities, voids remain reasonably spherical. Thus, in this limit a model with evolving voids shapes (full model) and the simpler model used here give very similar predictions. Calculations with the full model were performed for the high volume fraction composites analysed here. The predictions of the two models were very similar since regions of high triaxiality dominate the responses of these composites..

terms of the von-Mises effective Cauchy stress σ_e and the hydrostatic Cauchy stress $\sigma_m \equiv \sigma_{kk}/3$ as

$$\Phi \equiv \left(1+\frac{2}{3}f\right)\sigma_e^2 + \frac{9}{4}\left(\frac{1-f}{\ln f}\right)^2 \sigma_m^2 - (1-f)^2\sigma_Y^2 = 0, \tag{4.1}$$

where $\sigma_Y(\varepsilon_e^p)$ is the uniaxial yield strength of the plastic matrix material with zero porosity. The strain hardening response of the parent matrix material is assumed to be of the form

$$\sigma_Y = \sigma_0\left(1+\frac{\varepsilon_e^p}{\varepsilon_0}\right)^{1/N}, \tag{4.2}$$

where N is the hardening exponent, $\varepsilon_0 \equiv \sigma_0/[2(1+\nu_m)G_m]$ is the yield strain, and ε_e^p the von-Mises effective plastic strain in the parent solid material. Plastic normality is assumed with the matrix plastic strain rate given in terms of the plastic multiplier $\dot{\kappa}$ as

$$D_{ij}^p = \dot{\kappa}\frac{\partial \Phi}{\partial \sigma_{ij}}, \tag{4.3}$$

with the total strain rate taken as the sum of the elastic and plastic strain rates. The effective plastic strain rate in the matrix follows from a work balance (Gurson, 1977) as

$$\dot{\varepsilon}_e^p = \frac{\sigma_{ij}D_{ij}^p}{\sigma_Y(1-f)}, \tag{4.4}$$

which is integrated to give ε_e^p. It now remains to specify the evolution relation for the porosity f. Following Aravas and Ponte Castañeda (2004) we assume that the pore volume fraction is only affected by plastic deformation. Then recalling that the matrix absent of voids is plastically incompressible, the evolution rate of the pore volume fraction f is given as

$$\dot{f} = (1-f)D_{kk}^p, \tag{4.5}$$

which can be integrated knowing the plastic straining history and the initial porosity f_0 to obtain the current f.

We analyse the cubic periodic unit cell sketched in Fig. 9. It is subjected to periodic boundary conditions, such that the stress triaxiality $\Upsilon = -\bar{\sigma}_m/\bar{\sigma}_e$[‡] and Lode angle Θ defined as

$$\cos 3\Theta = \frac{27}{2}\frac{\det(\bar{\sigma}_{ij}')}{\bar{\sigma}_e^3}, \tag{4.6}$$

where $\bar{\sigma}_{ij}' = \bar{\sigma}_{ij} - \delta_{ij}\bar{\sigma}_{kk}/3$, are held fixed throughout the finite deformation loading. Here the overbar denotes the macroscopic stress quantities corresponding to the volume averages over the unit cell of the corresponding local quantities. Corresponding to the axisymmetric compression tests reported in Section 3.1, we fix $\Theta = 60^o$ and apply

[‡] We note that Υ is the stress triaxiality in terms of the Cauchy stress while η is the triaxiality in terms of the nominal stress. These two are approximately equal for the small macroscopic strains considered here but we denote them by different symbols to clarify this distinction.

volumetric average stresses $\bar{\sigma}_{33} \leq 0$ and $\bar{\sigma}_{11} = \bar{\sigma}_{22} \leq 0$ such that the stress state is axisymmetric about the $x_3 -$ axis (see Fig. 9 for definition of the co-ordinate system). This is achieved using the procedure described in Mbiakop et al. (2015) to keep Υ and Θ fixed.

Simulations are reported for $1/3 \leq \Upsilon \leq 1.0$. The material properties used in the simulations are as follows. The particles are modelled as essentially rigid compared to the matrix, consistent with the contrast between the matrix and particle phases in the idealised cermet. This is achieved by choosing a ratio $G_p/G_m = 10^3$ and $\nu_p = \nu_m = 0.3$. The matrix, absent of voids, is assumed to have a yield strain $\varepsilon_0 = 0.1\%$ and a hardening exponent $N = 10$. Moreover, unless otherwise stated, all calculations are presented for an initial porosity $f_0 = 10\%$ (recall that the idealised cermets have an overall porosity in the range 1-5%, which corresponds to a matrix porosity in the range 2.8% to 14%). All calculations were performed using the commercial finite element (FE) package Abaqus FEA and the unit cell discretised via 10-noded tetrahedral element (C3D10 in the Abaqus FEA notation) with a minimum element size $\sim 0.05D$, where D is the diameter of the spherical particles. The mesh is chosen to be denser in the narrow inter-particle channels, and coarser inside the elastic particles. All calculations are carried out in a finite strain setting.

We emphasise here that loading is specified in terms of the Cauchy stresses and the corresponding triaxiality Υ, consistent with stress measures employed in the porous matrix constitutive model. However, we present the stress predictions in terms of the 2nd Piola-Kirchhoff stress $\bar{S}_{ij} \equiv J\, \bar{F}_{ik}^{-1}\, \bar{\sigma}_{kl}\, \bar{F}_{jl}^{-1}$, where $\bar{F}_{ij}$ is the macroscopic deformation gradient (i.e. volume average of the deformation gradient over the unit cell) and $J \equiv \det(\bar{F}_{ij})$, in order to be consistent with the measurements discussed in Section 3.1. Correspondingly, the strains are presented in terms of the macroscopic Green-Lagrange strains $\bar{E}_{ij} \equiv 0.5(\bar{F}_{ki}\, \bar{F}_{kj} - \delta_{ij})$, which are work-conjugate to $\bar{S}_{ij}$. The macroscopic effective stresses and strains then follow the definitions in Section 2.

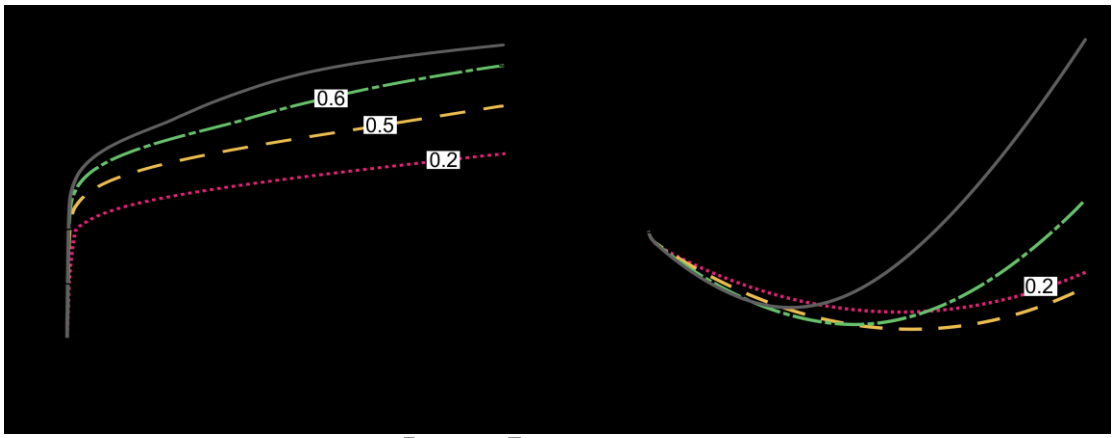

Figure 10: Predictions of the (a) $\bar{S}_e/\sigma_0 - \bar{E}_e$ response under uniaxial compression ($\eta = 1/3$) and (b) corresponding strain paths in $\bar{E}_m - \bar{E}_e$ space for the FCC unit cell with particle volume fractions in the range $0.2 \leq V_f \leq 0.65$ and initial matrix porosity $f_0 = 0.1$.

4.2 Summary of predictions for the periodic composites

Predictions of the $\bar{S}_e/\sigma_0 - \bar{E}_e$ responses under uniaxial compression ($\Upsilon = 1/3$) are plotted in Fig. 10a, with the corresponding strain paths in $\bar{E}_m - \bar{E}_e$ space included in Fig. 10b for particle volume fractions in the range $0.2 \leq V_f \leq 0.65$ and $f_0 = 0.1$. As expected, the strength increases with increasing V_f. More intriguingly, the strain paths show a qualitative change with increasing particle volume fraction. At low V_f, the composite undergoes volumetric compaction with the porosity in the matrix decreasing, consistent with the compressive mean stress associated with uniaxial compression. However, with increasing V_f, after an initial compaction phase the composite begins to dilate with $d\bar{E}_m/d\bar{E}_e > 0$ even under the imposed compressive mean stress. In fact, for the $V_f \geq 0.6$ composites, there is overall dilation on the order of 0.5% after deforming the composite to about $\bar{E}_e = 0.06$.

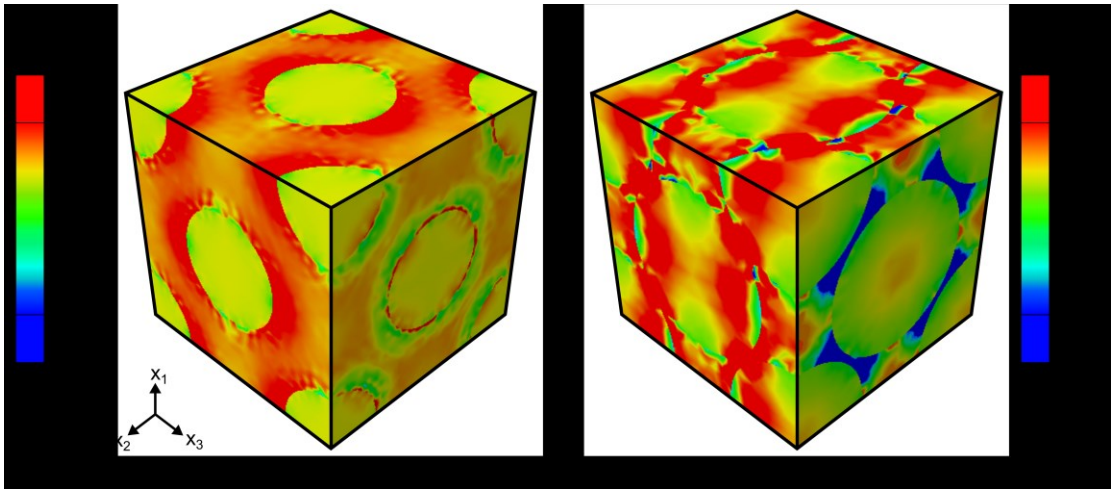

Figure 11: Predictions of spatial distribution of triaxiality v in the FCC unit cell with volume fractions (a) $V_f = 0.2$ and (b) $V_f = 0.65$ of spherical particles. Results are shown for the case of an initial porosity $f_0 = 0.1$ in the matrix with the unit cell subjected to uniaxial compression ($\Upsilon = 1/3$) to a strain $\bar{E}_e = 0.1$. Loading is axisymmetric about the x_3 −axis.

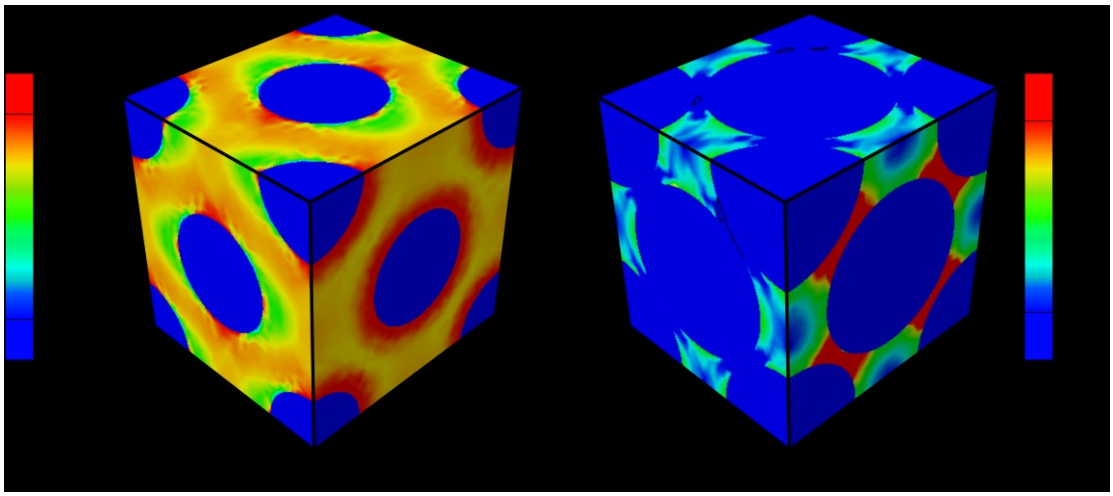

Figure 12: Predictions of spatial distribution of the porosity f in the matrix in the FCC unit cell with volume fractions (a) $V_f = 0.2$ and (b) $V_f = 0.65$ of spherical particles. Results are shown for the case of an initial porosity $f_0 = 0.1$ in the matrix with the unit cell subjected to uniaxial compression ($\Upsilon = 1/3$) to a strain $\bar{E}_e = 0.1$. Loading is axisymmetric about the x_3 −axis.

In order to understand these differences, we include in Figs. 11a and 11b spatial distributions of the stress triaxiality ($\upsilon \equiv -\sigma_m/\sigma_e$) within models with $V_f = 0.2$ and 0.65, at $\bar{E}_e = 0.07$. The stress state is more spatially homogeneous in the low volume fraction composite with $\upsilon > 0$. By contrast, at high volume fractions, υ is spatially very heterogeneous and there exist regions wherein $\upsilon < 0$ (i.e. tensile mean stresses) even though the macroscopic mean stress is compressive. These tensile mean stresses within the matrix result in the dilation of the matrix with an associated increase in the porosity. Contours of porosity, included in Fig. 12, show clearly that in the $V_f = 0.65$ composite there are regions with significant increases in the porosity at the prescribed deformation, whereas in the $V_f = 0.2$ composite, the porosity is seen to mainly decrease from this initial value. This high porosity is localised in between the thin inter-particle zones where the triaxiality is also higher. The increase in porosity in the $V_f = 0.65$ composite results in an overall dilation.

This general behaviour is strongly affected by the initial porosity f_0. Predictions of the variation of $\bar{E}_m$ with $\bar{E}_e$ for uniaxial compression of the $V_f = 0.6$[§] composite are included in Fig. 13 for $0.001 \leq f_0 \leq 0.1$. While the high porosity composites undergo initial compaction, this compaction phase is reduced or eliminated with decreasing porosity. On the other hand, $d\bar{E}_m/d\bar{E}_e$ is nearly independent of f_0 when the deformations as parameterised by $\bar{E}_e$ are large. This nevertheless implies that for a given $\bar{E}_e$ the overall levels of positive $\bar{E}_m$ are larger for composites with lower f_0 as seen in Fig. 13 as the compaction mode is penalised at low f_0.

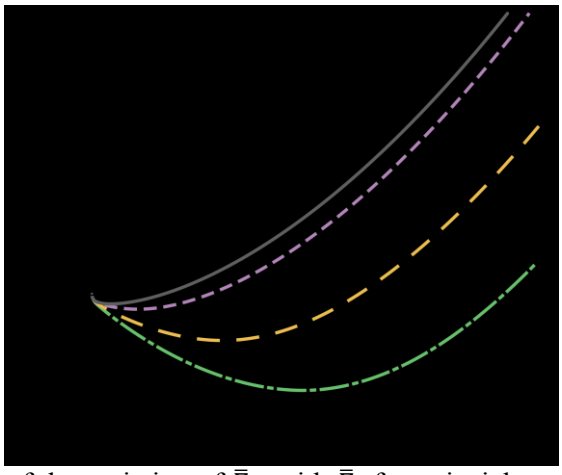

Figure 13: Predictions of the variation of $\bar{E}_m$ with $\bar{E}_e$ for uniaxial compression ($\Upsilon = 1/3$) of the $V_f = 0.6$ composite with the FCC unit cell. Results are shown for initial matrix porosities in the range $0.001 \leq f_0 \leq 0.1$.

Predictions of the $\bar{S}_e/\sigma_0 - \bar{E}_e$ responses of the $V_f = 0.6$ ($f_0 = 0.1$) composite with varying levels of triaxiality Υ are included in Fig. 14a, and corresponding strain paths in $\bar{E}_m - \bar{E}_e$ space are plotted in Fig. 14b. The corresponding measured $\bar{S}_e/\sigma_0 - \bar{E}_e$ responses are also included in Fig. 14a with the choice $\sigma_0 = 30$ MPa (Bele and Deshpande, 2015). There are some clear consistencies between measurements and

[§] Henceforth we restrict results to the $V_f = 0.6$ case for the high volume fraction composites. With increasing V_f, the thin matrix channels resulted in numerical convergence difficulties and a full set of results could not be obtained for $V_f > 0.6$.

predictions: (i) the stress-strain measurements and predictions are in remarkable agreement with the predictions capturing the increase in the hardening rate with increasing triaxiality and (ii) both predictions and measurements show a transition from dilation to compaction with increasing triaxiality, which is in qualitative agreement with experiments. Nevertheless, a clear quantitative discrepancy remains between the numerical predictions and measurements: the levels of predicted dilation at low stress triaxiality are relatively small compared to the analogous experimental results (compare Figs. 3b and 14b). This difference can be understood by recalling that the level of dilation increases with increasing V_f (Fig. 10b) due to the constraint imposed by the particle skeleton. While the particle volume fractions of these periodic models are approximately equal to those of the idealised cermets, there exists a key microstructural difference. The experimentally investigated cermets have a random packing of the spherical particles with particle-particle contacts forming force chains as discussed in Bele and Deshpande (2015) and Pickering et al. (2016). This imposes a strong kinematic constraint on the deformation mode, and we anticipate that similar to granular materials it results in relatively high macroscopic dilation.

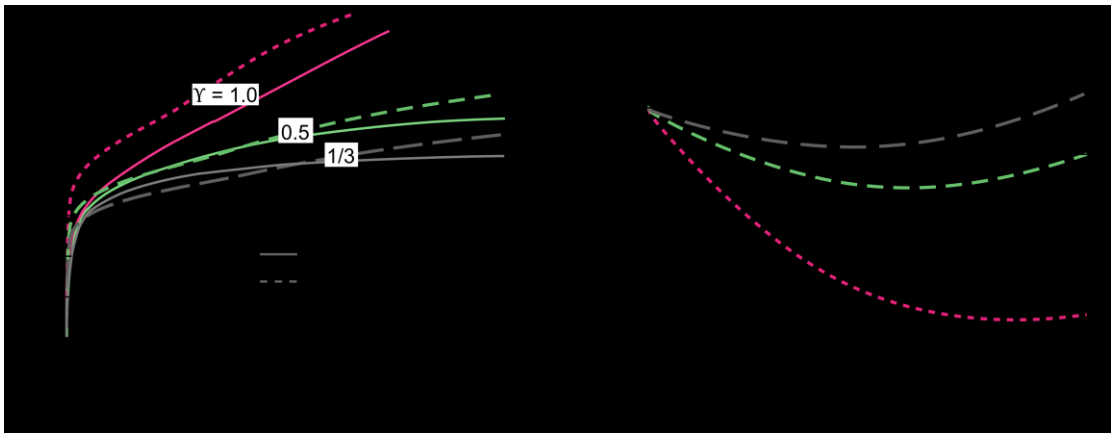

Figure 14: Predictions of the (a) $\bar{S}_e/\sigma_0 - \bar{E}_e$ responses and (b) corresponding strain paths in $\bar{E}_m - \bar{E}_e$ space for varying levels of triaxiality Y. The calculations use the FCC unit cell with particle volume fraction $V_f = 0.6$ and initial matrix porosity $f_0 = 0.1$. In (a) we include the corresponding measurements with the measured stresses normalised by the Sn/Pb solder matrix yield strength $\sigma_0 = 30$ MPa.

We note in passing here that the *conventional* porous plasticity model (i.e. model with no higher order terms such as gradients of plastic strain etc.) used to describe the matrix allows for large plastic strains to develop at the particle/matrix interfaces. In reality, the blockage of dislocation motion by the elastic particles will inhibit plastic straining near the interface (Danas et al., 2010) and thereby enhance the effective matrix strength. This strengthening effect due to the formation of a boundary layer at the interface is only significant in thin matrix films on the order of a few microns. While the roles of such higher order plasticity effects are not investigated here, the fact that the conventional plasticity model predicts the measured strength to reasonable level of accuracy (Fig. 14a) suggests that these effects play a minor role in the idealised cermets analysed here. By contrast, FE calculations performed as part of this study, but not shown here for the sake of brevity, suggest that de-bonding between the matrix and the particles significantly reduces the strength of the composite and increases the overall dilation levels. For instance, we found that for a composite with 60% volume particles, the uniaxial compressive strength of the de-bonded composite is about half that of the

composite with bonded particles but this de-bonded composite dilates to $\bar{E}_m \approx 0.02$ at a imposed strain $\bar{E}_e = 0.05$ whereas the corresponding dilation in the bonded composite is negligible.

The analysis of random composites with a high volume fraction of spherical particles, even though theoretically possible (see for instance Lopez-Pamies et al. (2013), albeit at lower particle volume fractions), is beyond the scope of current numerical tools for two reasons: the analysis will require (i) the modelling of large representative volume elements and many millions of degrees of freedom to adequately represent the porous matrix and the particles and (ii) the inclusion of the very thin matrix films in between particles that are touching each other; accurate FE modelling of the deformation of such thin porous films that undergo very large local deformations further complicates the FE modelling. A more appropriate discrete particle model is presented in the following section that is free of such disadvantages.

5. Analysis of the deformation of a random assembly of spherical particles

The periodic regular composite analysed in Section 4 does not adequately capture the kinematic constraints imposed by the particle skeleton. Hence in order to understand the kinematics of idealised cermets, we analyse the response of a model comprising a random aggregate of densely packed particles, with no matrix filling the interstitial sites (i.e. a so-called discrete element model). This approximation thus represents the other extreme, i.e. we model the constraints due to the particle skeleton but do not accurately account for the constraints imposed by the matrix.

5.1 Brief description of model

Here we analyse a "full specimen" rather than a RVE. The specimen is a cuboid of height H and square cross-section of side length $H/2$, containing randomly packed spherical particles of diameter $D \approx H/12$ as shown in Fig. 15a. The particles are packed using the Lubachevsky-Stillinger algorithm (Lubachevsky and Stillinger, 1990), which has been used extensively to simulate random packing of objects within boundary walls. Within the cuboidal box, 400 spheres are packed to a volume fraction $V_f \approx 0.6$. Both tensile and compressive inter-particle forces are modelled, in order to ensure the stability of the assembly under hydrostatic and deviatoric applied stress states. The contact model sketched in Fig. 15b defines these forces. Such a modelling scheme is commonly referred to in the literature as a "discrete element" simulation.

The contact law between particles is defined as follows. An elastic-plastic truss (i.e. a strut that can carry tensile and compressive loads but no shear or bending loads) of cross-sectional area A_T, tensile yield strength Σ_T, compressive yield strength Σ_C and Young's modulus Y_T connects the centres of each neighbouring particle. The undeformed length of the truss (i.e. state when the truss carries no force) is its length in the initial undeformed configuration of the assembly with the truss exerting either compressive or tensile forces between the connecting particles as it is shortened or lengthened, respectively from this initial state. In order to represent the full kinematic constraint of the particles, we also include a soft contact particle model along the lines of the model introduced by Cundall and Strack (1979). This contact model is included in the sketch in Fig. 15b. Briefly, with r as the distance of separation of the particle centres, and the particle interpenetration given by $\delta_n = r - D$, the normal contact force during active contact ($\delta_n < 0$) is given by $F_n = K_n \delta_n$ so that the total contact force

equals the contact force F_n and the force exerted by the truss. A tangential force F_s between the particles also only exists during an active contact, and opposes sliding. It is limited in magnitude to $|F_s| < \mu|F_n|$, where μ is the friction coefficient. This frictional force F_s is defined by an elastic-plastic Coulomb type relation with stiffness K_s, i.e.

$$F_s = \begin{cases} K_s \dot{\delta}_s & \text{if } |F_s| < \mu|F_n| \text{ or } F_s\dot{\delta}_s < 0, \\ 0 & \text{otherwise} \end{cases} \tag{5.1}$$

with $\dot{\delta}_s$ defined as the tangential displacement rate between the contacting particles. Unless otherwise specified, all calculations are presented with $K_n = 70Y_T A_T/D$, $K_s = 2/7K_n$, $\mu = 0.6$, $\Sigma_C = Y_T/100$ and $\Sigma_T/\Sigma_C = 1$. The purpose of this model is only to investigate the kinematics and does not attempt to predict the stress versus strain response. While the absolute values of these strengths and stiffnesses do not affect the kinematics, for completeness we mention that the calculations used a relatively low truss strength $\Sigma_C = 10$ MPa.

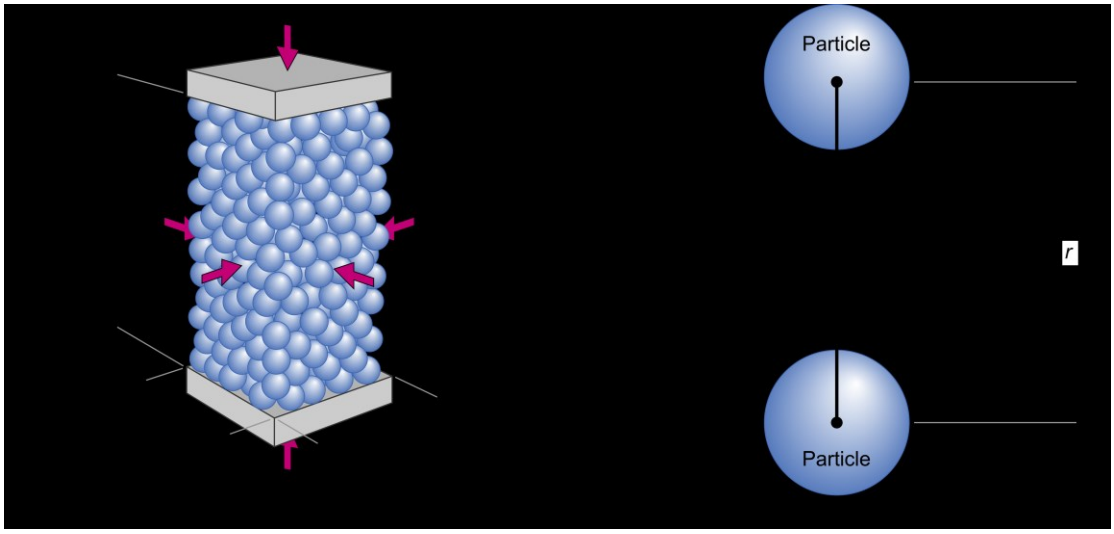

Figure 15: (a) The assembly of 400 spherical particles forming a cuboidal specimen of height H and base $H/2 \times H/2$ analysed using discrete element simulations. Axisymmetric loading about the $x_3 -$ axis was applied by compressing the specimen between the rigid platens included in the sketch. (b) Sketch of the inter-particle contact model used in the simulations.

Similar to the experiments reported in Section 3, the cuboidal specimen (Fig. 15a) analysed here was subjected to axisymmetric loading about the $x_3 -$ axis with proportional stress paths. This loading was imposed as follows. The specimen was compressed in the $x_3 -$ direction between two rigid platens as shown in Fig. 15a. All displacement degrees of freedom were constrained on the bottom platen, while in the top platen all rotations, and translations in the x_1 and x_2 directions, were constrained. The top platen was compressed against the specimen by the application of a compressive force F_3 in the $x_3 -$ direction such that the nominal axial stress $\bar{N}_{33} = 4F_3/H^2$, with F_3 defined to be negative in compression. Further, a non-sliding frictional constraint was imposed on the particles in contact with both the platens, i.e. the translation in the $x_1 - x_2$ plane of particles in contact with the platens was constrained. The specimen was subjected to an axisymmetric stress state by specifying that the

nominal stresses $\bar{N}_{11} = \bar{N}_{22}$. These stresses are related to the axial stress via the triaxiality η via

$$\bar{N}_{11} = \bar{N}_{22} = \frac{3\eta + 1}{3\eta - 2}\bar{N}_{33}. \tag{5.2}$$

Note that here we use the symbol η to denote triaxiality, as it is defined in a manner analogous to the experiments in terms of the nominal stresses. The forces on the lateral surfaces with outward normal n_j (in the undeformed configuration) that generate these nominal stresses $\bar{N}_{11}$ and $\bar{N}_{22}$ are given as

$$F_i = \frac{H^2}{2}\bar{N}_{ij}n_j. \tag{5.3}$$

This total force is distributed equally over all particles on that lateral outer surface, i.e. a force $f_i = F_i/K$ is applied at the centre of each of the K surface particles on the respective lateral surface. This scheme ensures that the specimen is subjected to proportional axisymmetric stressing with overall force equilibrium guaranteed and moment equilibrium satisfied by the force distributions generated by the contact of the specimen with the rigid platens on the top and bottom surfaces.

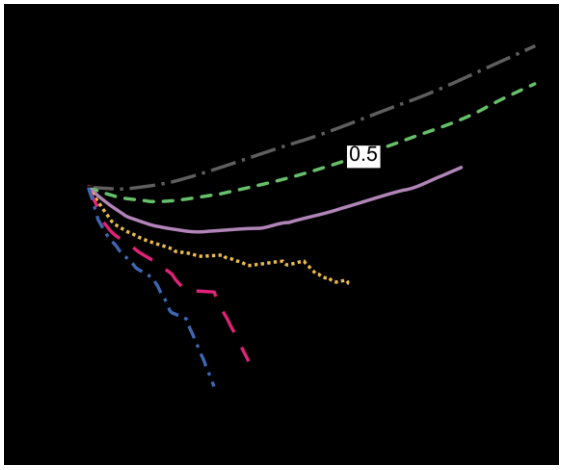

Figure 16: Discrete element predictions of the variation of the macroscopic strains $\bar{E}_m$ and $\bar{E}_e$ for varying levels of triaxiality η.

The main aim of this model is to predict both the overall deformation state and also the distribution of deformation within the specimen. The local "strains" within the assembly are defined as follows. The domain is discretised into linear (i.e. 4-noded) tetrahedral elements with the nodes at the centres of the particles. The displacements at the four nodes of the tetrahedra along with their associated shape functions in the undeformed configuration are used to calculate the deformation gradient $F_{ij}^{(k)}$ within element (k) and the corresponding Green-Lagrange strain $E_{ij}^{(k)} \equiv 0.5(F_{ki}^{(k)}F_{kj}^{(k)} - \delta_{ij})$. The volume averaged deformation gradient over the M tetrahedral elements with the specimen then follows as

$$\bar{F}_{ij} \equiv \frac{1}{V_0}\sum_{k=1}^{M} V^{(k)}F_{ij}^{(k)}, \tag{5.4}$$

where $V_0 = \sum_{k=1}^{M} V^{(k)}$ with $V^{(k)}$ the undeformed volume of element (k). In the following we discuss distributions of the volumetric and effective strains $E_m^{(k)}$ and $E_e^{(k)}$, respectively defined in a manner analogous to the DVC analysis of Section 3.2. We

emphasise here that E_{ij} is not the strain in the matrix or the particles but rather a measure of the average strain in the tetrahedron comprising both matrix and particles. The corresponding macroscopic average strains $\bar{E}_{ij}$ as well as $\bar{E}_m$ and $\bar{E}_e$ are defined from $\bar{F}_{ij}$ as detailed in Section 4.1. We note in passing that the non-linear definition of the Green-Lagrange strain implies that $\bar{E}_{ij}$ is *not* equal to the volume average of $E_{ij}^{(k)}$.

5.2 Deformation fields and effect of triaxiality

Predictions of the variation of $\bar{E}_m$ with $\bar{E}_e$ are plotted in Fig. 16 for selected triaxialities η. Consistent with observations (Fig. 3b) and predictions of the periodic model (Fig. 14b), the levels of dilation increase with decreasing triaxiality η and the aggregate undergoes overall compaction at the higher triaxialities over the range of deformations considered here. However, unlike the periodic model of Section 4, the levels of dilation are now significantly higher for the low triaxialities and similar to those seen in the measurements. This confirms our initial hypothesis that at a relatively high particle volume fraction, a random particle arrangement invariably implies percolated particle chains, and results in kinematic constraints that give rise to high levels of dilation at low triaxialities.

Three-dimensional views of the specimen showing distributions of E_m and E_e are included in Figs. 17 and 18, respectively. The views are shown at four levels of applied strain $\bar{E}_e$ and for three values of η (the two largest values of $\bar{E}_e$ are omitted for the highest triaxiality of $\eta = 1.5$ as those calculations encountered numerical convergence difficulties). First consider the distributions of E_m. At low levels of overall deformation ($\bar{E}_e = 0.02$), regions of both compaction and dilation are observed for all values of η. With increasing deformation, regions of dilation dominate for the $\eta = 1/3$ case while regions of compaction dominate for $\eta = 1.5$. This is consistent with the overall levels of $\bar{E}_m$ seen in Fig. 16 but nevertheless it is worth emphasising that regions of compaction and dilation are observed for both $\eta = 1/3$ and 1.5 at all levels of $\bar{E}_e$, in line with the DVC measurements reported in Section 3.2. By contrast the distributions of E_e are reasonably similar for the three triaxialities η included in Fig. 18.

To further illustrate the observation that the kinematic response of a region within the specimen is dependent on the macroscopic stress triaxiality, we consider in Fig. 19 the evolution of E_m with the overall deformation $\bar{E}_e$ for three tetrahedra within the specimen. Results in Fig. 19 are shown for the $\eta = 1/3$ and 1.5 cases and exemplifies the complexity of the kinematics. Tetrahedra labelled (i) and (ii) in Fig. 19 switched from dilatory paths to compactive paths as triaxiality was changed from $\eta = 1/3$ to 1.5 while the tetrahedron labelled (iii) dilated for deformation with $\eta = 1.5$ but slightly compacted with $\eta = 1/3$.

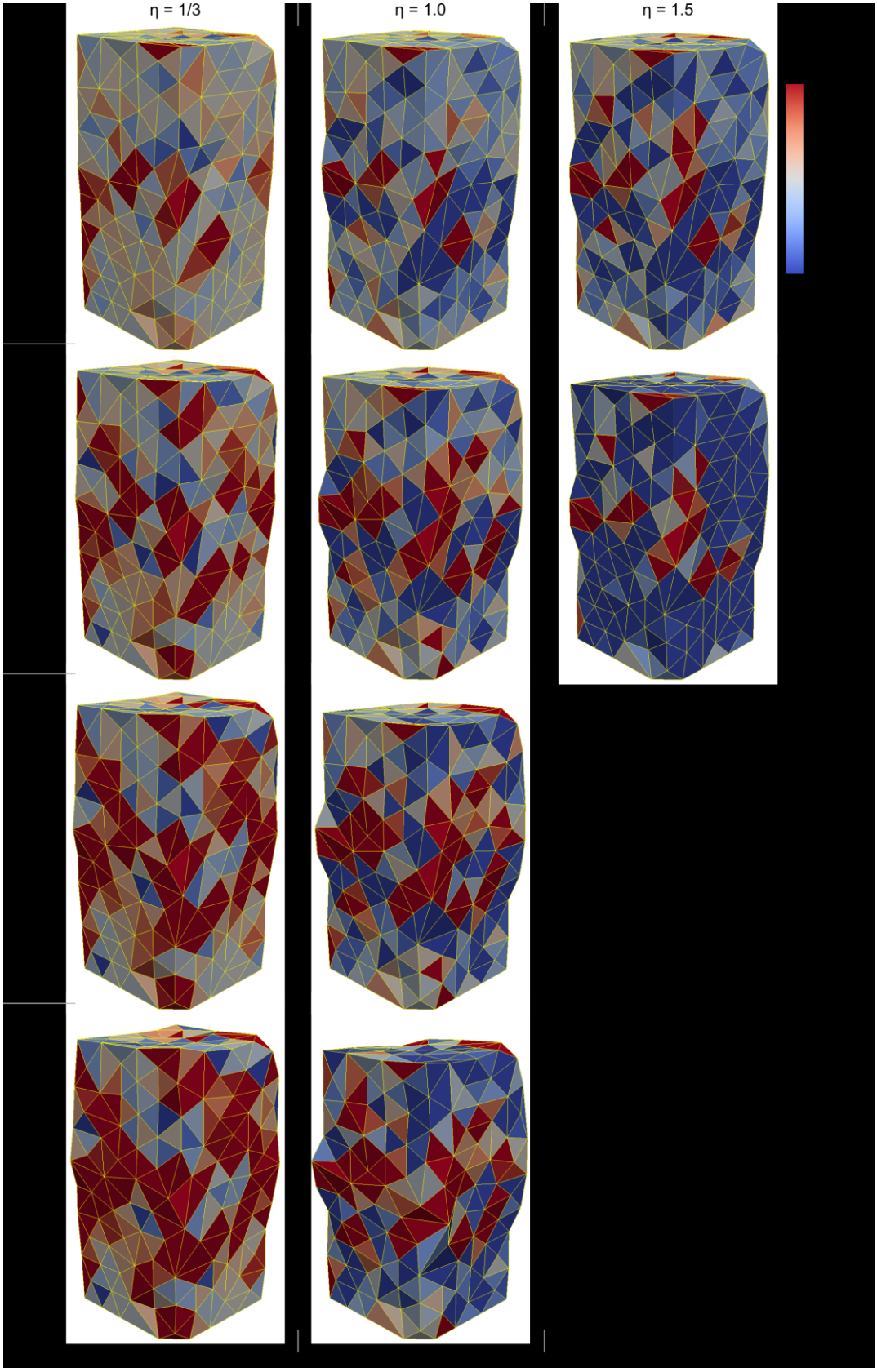

Figure 17: Discrete element predictions of the spatial distribution of the volumetric strain E_m (shown on the deformed configurations) in the idealised cermet specimen at selected applied macroscopic strains $\bar{E}_e$. Results are shown for three stress paths (a) $\eta = 1/3$, (b) $\eta = 1.0$ and (c) $\eta = 1.5$. The numerical simulations did not converge for $\bar{E}_e > 4\%$ for $\eta = 1.5$ and hence those cases are omitted in (c).

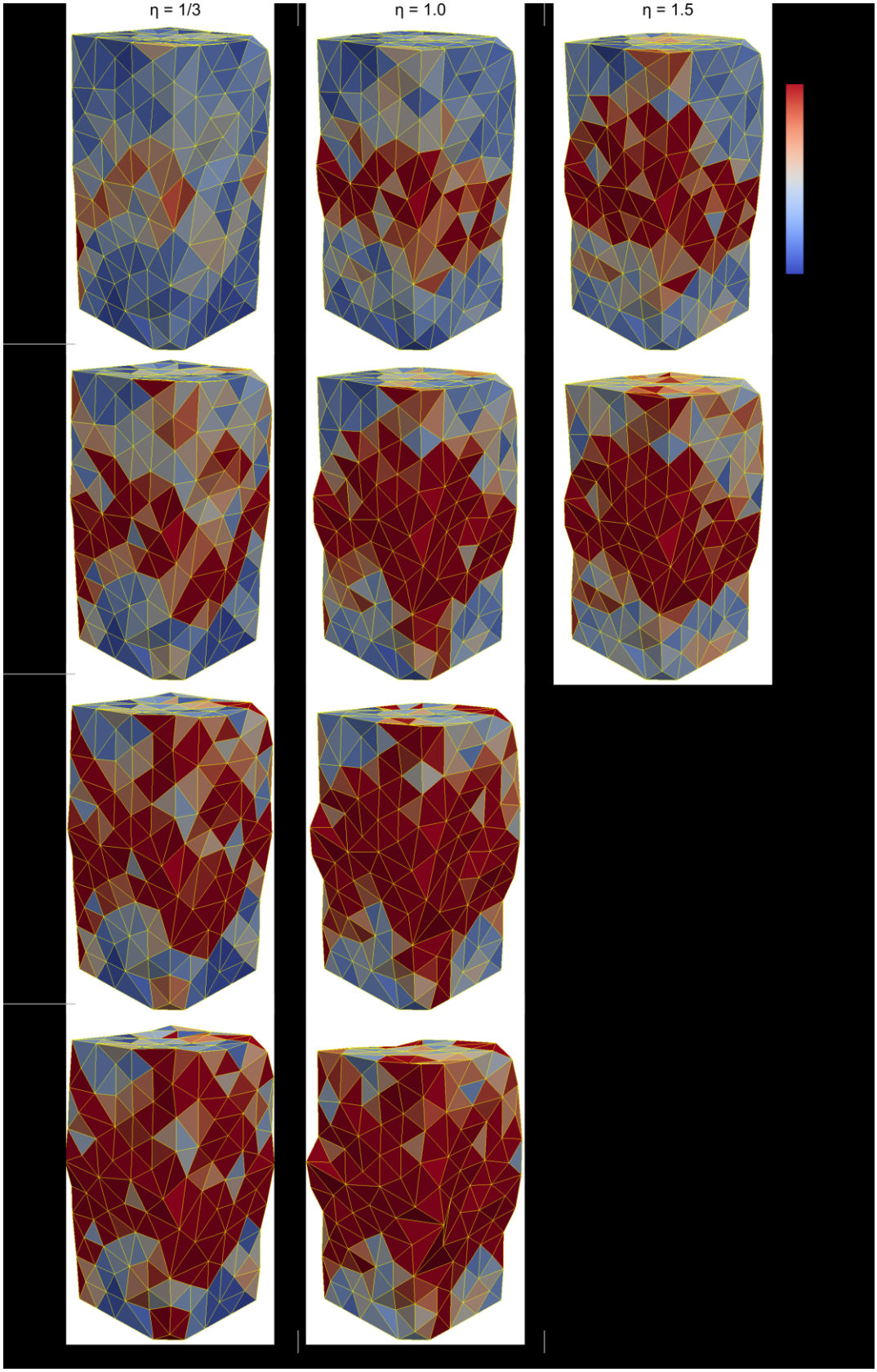

Figure 18: Discrete element predictions of the spatial distribution of the effective strain E_e (shown on the deformed configurations) in the idealised cermet specimen at three applied macroscopic strains $\bar{E}_e$. Results are shown for three stress paths (a) $\eta = 1/3$, (b) $\eta = 1.0$ and (c) $\eta = 1.5$. The numerical simulations did not converge for $\bar{E}_e > 4\%$ for $\eta = 1.5$ and hence those cases are omitted in (c).

While the dependence of local particle kinematics on the macroscopic stress state is relatively complex, the trends of the collective response are clear from Fig. 16: the specimen undergoes less dilation and even compaction with increasing triaxiality. This suggests that with increasing triaxiality, a larger fraction of the specimen is compacting rather than dilating. In order to quantify this, we define a dilated volume fraction as

$$\phi = \frac{1}{V_0}\sum_{k=1}^{M} V^{(k)}\,\mathcal{H}[\,E_m^{(k)}], \tag{5.5}$$

where $\mathcal{H}[\cdot]$ is a Heaviside step function. The variation of ϕ with $\bar{E}_e$ is included in Fig. 20 for $\eta = 1/3$ and $\eta = 1.5$: clearly ϕ is significantly higher at the lower triaxiality value. Moreover, while ϕ is nearly monotonically increasing with $\bar{E}_e$ for $\eta = 1/3$, the ϕ versus $\bar{E}_e$ relation fluctuates at $\eta = 1.5$ as regions of the specimen compact and dilate alternatively during different stages in the deformation.

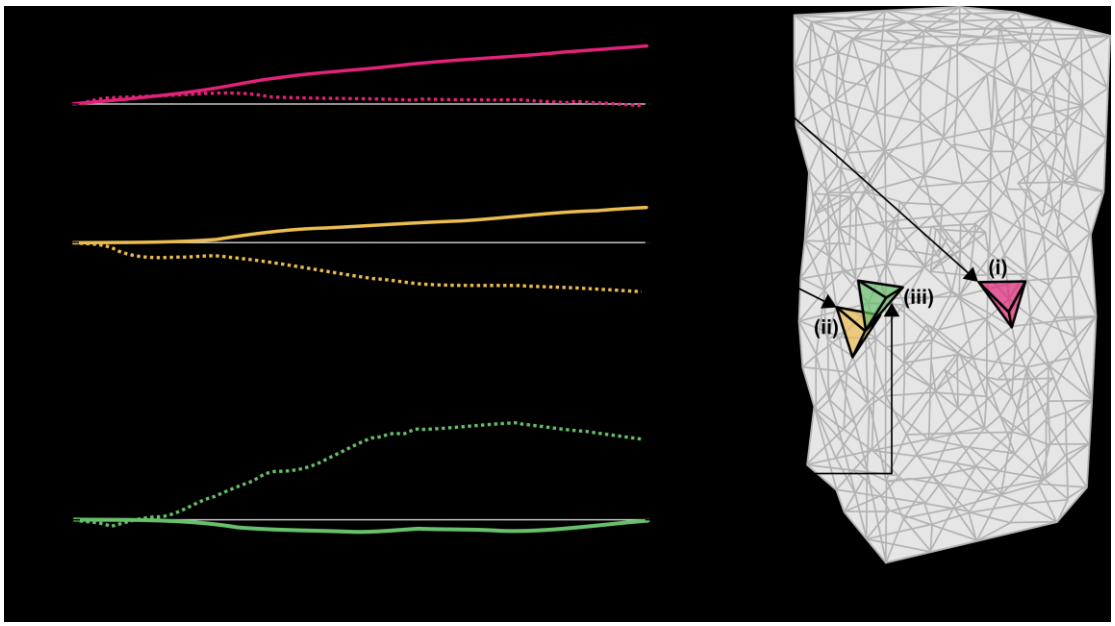

Figure 19: Discrete element predictions of the evolution of the mean strain E_m with the macroscopic strain $\bar{E}_e$ in three selected tetrahedra within the assembly of spherical particles analysed here. The three tetrahedra are indicated in the specimen and the $E_m - \bar{E}_e$ curves shown for $\eta = 1/3$ and $\eta = 1.5$.

5.3 Effect of inter-particle contact properties

The differences in the local kinematic response to the imposed stress triaxiality are related to the relative constraints against compaction and dilation, and can be understood in a qualitative manner as follows. For the purpose of this discussion assume that there are two modes whereby a local region can be deformed to a given level of E_e: a dilatory and a compaction mode. The dilatory mode is inhibited with increasing triaxiality as the mode involves work done against the externally applied pressure, with the compaction mode becoming more favourable as seen in the results presented above. Moreover, increasing the internal constraints can also inhibit the dilatory mode. For example, an incompressible matrix filling all the interstitial gaps between the particles will significantly reduce the tendency of the system to dilate, with the dilation mode only activated if the tensile hydrostatic stress within the matrix exceeds the cavitation pressure. In order to illustrate the effect of varying the level of the dilatory and

compaction constraints, we report here calculations with unequal compressive and tensile yield strengths: viz. the tensile truss yield strength Σ_T is decreased from $\Sigma_T = \Sigma_C$ to $\Sigma_C/\Sigma_T = 100$ while keeping all other particle contact properties unchanged from the reference values detailed in Section 5.1.

Predictions of the variation of ϕ with $\bar{E}_e$ are included in Fig. 20 for $\Sigma_C/\Sigma_T = 10$ and 100 in addition to the reference value of $\Sigma_C/\Sigma_T = 1$ for both $\eta = 1/3$ and 1.5. With increasing Σ_C/Σ_T, the dilated fraction ϕ clearly increases at $\eta = 1/3$, due to the fact that the lower tensile truss strength favours the dilatory mode over the compaction mode. A similar increase is also observed for $\eta = 1.5$ but the changes are relatively small as only a small fraction of the specimen dilates at this high triaxiality.

It is thus evident that a full quantitative prediction of the response of the idealised cermets reported in Section 3 will require not only the accurate capture of the constraint imposed by the porous matrix (using formulations as in Section 4) but also the analysis of large RVEs with a high volume fraction of randomly packed spheres that include the constraints on the kinematics imposed by the contact of the particles. Such an analysis is beyond the scope of current computational capability but the limiting models presented here reveal some key physics and illustrate the limitations of these simplified models.

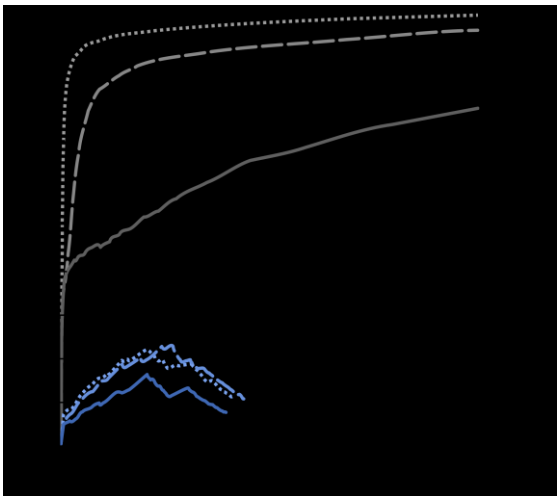

Figure 20: Discrete element predictions of the fraction ϕ of the specimen that undergoes dilation, as a function of the macroscopic strain $\bar{E}_e$ for two selected values of the triaxiality η. In each case we show results for the reference value of $\Sigma_C/\Sigma_T = 1$ and two additional values of Σ_C/Σ_T.

6. Concluding remarks

The response of idealised cermets comprising approximately 60% by volume steel spheres in a Sn/Pb solder matrix is investigated under a range of axisymmetric compressive stress states. The measured macroscopic stress-strain responses, and digital volume correlation (DVC) analyses revealed two distinct deformation mechanisms. At low triaxialities, the cermets behave as granular media and dilate under compressive loading. This gives rise to an increasing hardening rate with increasing triaxiality. By contrast, at sufficiently high triaxialities the deformation switches to a macroscopically incompressible mode, resulting in a stress versus strain response that is independent of triaxiality. However, the DVC reveals that under all triaxialities there

are local regions with dilatory and compaction responses; the magnitude of dilation and the number of zones wherein dilation occurs decreases with increasing triaxiality.

Two numerical models are presented in order to understand these mechanisms: (i) a FCC periodic unit cell model comprising nearly rigid spherical particles in a porous metal matrix and (ii) a discrete element model comprising a large random aggregate of spheres connected by non-linear normal and tangential "springs". The periodic unit cell model captures the measured stress-strain response with reasonable accuracy but significantly under-predicts the observed dilation at the lower triaxialities. While this model does predict overall dilation at low triaxialities, it under-predicts the magnitude of the dilation significantly because the non-contacting particles in this model underestimate the kinematic constraints imposed by the percolated particle chains in the idealised cermets.

By contrast, the discrete element model captures the kinematics and predicts not only the overall levels of dilation but also the fact that both local compaction and dilatory regions exist for all triaxialities. However, this model does not explicitly include the matrix and it is unclear how the inter-particle contact law can be directly connected to the matrix properties. Thus, the model cannot be used as a predictive tool for the overall stress versus strain responses of idealised cermets.

The analyses reported here have revealed that the complete constitutive response of cermets depends sensitively on both the kinematic constraints imposed by the particle aggregate skeleton and the constraints imposed by the metal matrix filling the interstitial spaces in that skeleton. It is thus evident that a full quantitative prediction of the response of the idealised cermets will require the analysis of large RVEs comprising a high volume fraction of randomly packed spheres within a porous plastic matrix. While such an analysis is beyond the scope of current computational capability, the limiting models presented here reveal some key physics of the deformation mechanisms of cermets.

Appendix A: Volumetric and deviatoric strains for Green-Lagrange strain measures

Throughout the main body of the paper we have used Green-Lagrange strain measures. This is because local strains and rotations within the idealised cermets might be large and thus it is most convenient to illustrate the deformations as measured by the DVC analysis via a finite strain measure such as the Green-Lagrange strain measure. Further, for simplicity, we then used $E_m\delta_{ij}$ and $E'_{ij} = E_{ij} - E_m\delta_{ij}/3$ to parameterise the volumetric and deviatoric strains, respectively. These measures were motivated from the analogous small strain definitions but are not precise in the finite strain context.

While the decomposition $E_{ij} = E'_{ij} + E_m\delta_{ij}/3$ ensures that E'_{ij} is trace-less it is not a deviatoric strain in the sense of representing a deviation from the volumetric strain. This is because E_m is not the Green-Lagrange volumetric strain. An alternative decomposition suggested by Bažant (1996) is

$$E_{ij} = E^d_{ij} + \delta_{ij}E_v/3, \tag{A1}$$

with

$$E_v = 3\left(E_0 + \frac{1}{2}E_0^2\right), \tag{A2}$$

where $E_0 \equiv J^{1/3} - 1$ with $J = \det(F_{ij})$ and F_{ij} the deformation gradient. With this decomposition $\delta_{ij}E_v/3$ is the Green-Lagrange strain tensor for purely volumetric deformations and therefore E_{ij}^d is a deviatoric strain tensor (i.e. vanishes for purely volumetric deformation). However, now E_{ij}^d is no longer trace-less as is the case with small strain measures of the deviatoric strain tensor. We can then define a measure of the deviatoric deformation analogous to the von-Mises effective strain as

$$E_{eq} \equiv \sqrt{\frac{2}{3}E_{ij}^d E_{ij}^d}, \tag{A3}$$

and decompositions of the average strain measures $\bar{E}_{ij}$ follow analogous definitions. The data in Fig. 3b for $\eta = 1/3$, 0.75, 1 and 1.5 is re-plotted in Fig. A1a as $\bar{E}_v$ versus $\bar{E}_{eq}$ with the data in terms of $\bar{E}_m$ versus $\bar{E}_e$ also included for comparison purposes. The differences are relatively small over the full range of strains investigated here.

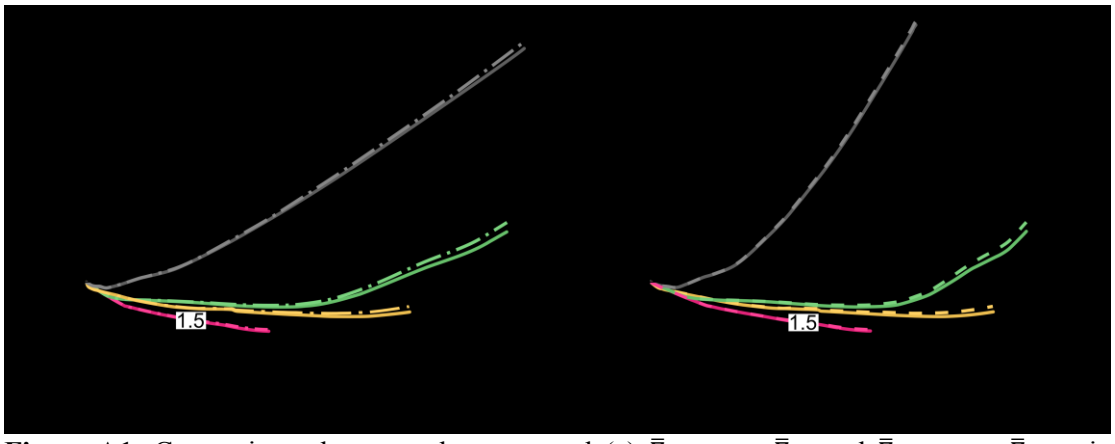

Figure A1: Comparisons between the measured (a) $\bar{E}_v$ versus $\bar{E}_{eq}$ and $\bar{E}_m$ versus $\bar{E}_e$ strain curves and (b) $\Delta V/V_0$ versus $\bar{E}_a$ and $\bar{E}_m$ versus $\bar{E}_a$ curves for the idealised cermets. Curves are shown here for four values of η using the data from Fig. 3b.

We emphasise that while $\bar{E}_v\delta_{ij}$ is a volumetric tensor, neither $\bar{E}_v$ nor $\bar{E}_m$ gives the volumetric strain defined as $\Delta V/V_0$, where ΔV and V_0 are the change in volume and initial volumes, respectively of the specimen. To illustrate this we re-plot in Fig. A1b the data of Fig. 3b in terms of $\Delta V/V_0 = J - 1$ versus $\bar{E}_a$ along with $\bar{E}_m$ also versus $\bar{E}_a$. Again, we can see that the differences between $\bar{E}_m$ and $\Delta V/V_0$ are relatively small even at the highest levels of deformation investigated here. Similar small discrepancies are also seen between $\bar{E}_v$ and $\Delta V/V_0$ (omitted here for the sake of brevity). We thus conclude that for strain levels investigated here the simple measures of volumetric and deviatoric deformations motivated by small strain definitions suffice but we anticipate significant differences to emerge at larger strains.

Acknowledgements
The authors are grateful to the Office of Naval Research (ONR) for their financial support through grant number N000141210637 on Nickel bonded TiC composites for

dynamic blast mitigation applications (program manager Dr. David Shifler). We also acknowledge the μ-VIS centre at the University of Southampton for provision of tomographic imaging facilities, supported by EPSRC grant EP-H01506X.

References

Aravas, N., Castañeda, P.P., 2004. Numerical methods for porous metals with deformation-induced anisotropy. Computer methods in applied mechanics and engineering 193, 3767–3805. doi:10.1016/j.cma.2004.02.009

Arsenault, R.J., Taya, M., 1987. Thermal residual stress in metal matrix composite. Acta Metallurgica 35, 651–659. doi:10.1016/0001-6160(87)90188-X

ASTM Committee C-21, 1955. Report of Task Group B on Cermets. American Society for Testing and Materials, Philadelphia.

Bao, G., Hutchinson, W., McMeeking, R.M., 1991. Plastic reinforcement of ductile materials against plastic flow and creep. Acta Metall. Mater 39, 1871–1882. doi:10.1016/0956-7151(91)90156-U

Bardenhagen, S.G., Brackbill, J.U., 1998. Dynamic stress bridging in granular material. Journal of Applied Physics 83, 5732. doi:10.1063/1.367429

Bay, B.K., Smith, T.S., Fyhrie, D.P., Saad, M., 1999. Digital volume correlation: Three-dimensional strain mapping using X-ray tomography. Experimental Mechanics 39, 217–226. doi:10.1007/BF02323555

Bažant, Z.P., 1996. Finite strain generalization of small-strain constitutive relations for any finite strain tensor and additive volumetric-deviatoric split. International Journal of Solids and Structures 33, 2887–2897. doi:10.1016/0020-7683(96)00002-9

Bele, E., Deshpande, V.S., 2015. The Compressive Response of Idealized Cermetlike Materials. Journal of Applied Mechanics 82. doi:10.1115/1.4029782

Blumenthal, W.R., Gray III, G.T., Claytor, T.N., 1994. Response of aluminium-infiltrated boron carbide cermets to shock wave loading. Journal of Materials Science 29, 4567–4576.

Budiansky, B., 1965. On the elastic moduli of some heterogeneous materials. Journal of the Mechanics and Physics of Solids 13, 223–227. doi:10.1016/0022-5096(65)90011-6

Cai, W., McDowell, G.R., Airey, G.D., 2013. Discrete element modelling of uniaxial constant strain rate tests on asphalt mixtures. Granular Matter 15, 163–174. doi:10.1007/s10035-013-0396-x

Castañeda, P.P., 1991. The effective mechanical properties of nonlinear isotropic composites. Journal of the Mechanics and Physics of Solids 39, 45–71. doi:10.1016/0022-5096(91)90030-R

Christman, T., Needleman, A., Suresh, S., 1989. An experimental and numerical study of deformation in metal-ceramic composites. Acta Metallurgica 37, 3029–3050. doi:10.1016/0001-6160(89)90339-8

Collop, A.C., McDowell, G.R., Lee, Y., 2007. On the use of Discrete Element Modelling to simulate the viscoelastic deformation behaviour of an idealised asphalt mixture. Geomechanics and Geoengineering 6025, 37–41. doi:10.1080/17486020701243128

Compton, B.G., Zok, F.W., 2013. Impact resistance of TiC-based cermets. International Journal of Impact Engineering 62, 75–87. doi:10.1016/j.ijimpeng.2013.06.008

Cundall, P.., Strack, O.D.., 1979. Discrete Numerical-Model for Granular Assemblies. Géotechnique 29, 47–65.

Danas, K., Deshpande, V.S., Fleck, N.A., 2010, Compliant interfaces: a mechanism for relaxation of dislocation pile-ups in a sheared single crystal, International Journal of Plasticity, 26, 1792-1805.

Danas, K., Aravas, N., 2012. Numerical modeling of elasto-plastic porous materials with void shape effects at finite deformations. Composites Part B: Engineering 43, 2544–2559. doi:10.1016/j.compositesb.2011.12.011

Deshpande, V.S., Cebon, D., 1999. Models of particle reinforced nonlinear-viscous

composite. Journal of Engineering Mechanics 125, 255–262.
Desrues, J., Chambon, R., Mokni, M., Mazerolle, F., 1996. Void ratio evolution inside shear bands in triaxial sand specimens studied by computed tomography. Géotechnique 46, 529–546. doi:10.1680/geot.1996.46.3.529
Desrues, J., Lanier, J., Stutz, P., 1985. Localization of the deformation in tests on sand sample. Engineering Fracture Mechanics 21, 909–921. doi:10.1016/0013-7944(85)90097-9
Drucker, D.C., Prager, W., 1952. Soil mechanics and plastic analysis for limit design. Quarterly of Applied Mathematics 10, 157–165.
Engqvist, H., Jacobson, S., Axén, N., 2002. A model for the hardness of cemented carbides. Wear 252, 384–393. doi:10.1016/S0043-1648(01)00866-3
Fang, Z.Z., 2005. Correlation of transverse rupture strength of WC–Co with hardness. International Journal of Refractory Metals and Hard Materials 23, 119–127. doi:10.1016/j.ijrmhm.2004.11.005
Finno, R.J., Harris, W.W., Mooney, M.A., Viggiani, G., 1997. Shear bands in plane strain compression of loose sand. Géotechnique 47, 149–165. doi:10.1680/geot.1997.47.1.149
Gillard, F., Boardman, R., Mavrogordato, M., Hollis, D., Sinclair, I., Pierron, F., Browne, M., 2014. The application of digital volume correlation (DVC) to study the microstructural behaviour of trabecular bone during compression. Journal of the Mechanical Behavior of Biomedical Materials 29, 480–499. doi:10.1016/j.jmbbm.2013.09.014
Gurson, A.L., 1977. Continuum theory of ductile rupture by void nucleation and growth. Journal of engineering materials and technology 99, 2–15.
Gustafson, T.W., Panda, P.C., Song, G., Raj, R., 1997. Influence of microstructural scale on plastic flow behavior of metal matrix composites. Acta Materialia 45, 1633–1643. doi:10.1016/S1359-6454(96)00277-7
Hashin, Z., Shtrikman, S., 1962. A variational approach to the theory of the elastic behaviour of polycrystals. Journal of the Mechanics and Physics of Solids 10, 343–352. doi:10.1016/0022-5096(62)90005-4
Hershey, A.., 1954. The Plasticity of an Isotropic Aggregate of Anisotropic Face-Centered Cubic Crystals. Journal of Applied Mechanics 21, 241–249.
Hill, R., 1965. A self-consistent mechanics of composite materials. Journal of the Mechanics and Physics of Solids 13, 213–222. doi:10.1016/0022-5096(65)90010-4
Hu, Z., Luo, H., Bardenhagen, S.G., Siviour, C.R., Armstrong, R.W., Lu, H., 2015. Internal Deformation Measurement of Polymer Bonded Sugar in Compression by Digital Volume Correlation of In-situ Tomography. Experimental Mechanics 55, 289–300. doi:10.1007/s11340-014-9856-4
Lopez-Pamies O., Goudari. T., Danas, K. 2013. The nonlinear elastic response of suspensions of rigid inclusions in rubber: II - A simple explicit approximation for finite-concentration suspensions, Journal of the Mechanics and Physics of Solids, 61, 19–37.
Lee, H.C., Gurland, J., 1978. Hardness and deformation of cemented tungsten carbide. Materials Science and Engineering 33, 125–133. doi:10.1016/0025-5416(78)90163-5
Lee, J., Kim, N.J., Jung, J.., Lee, E.-S., Ahn, S., 1998. The influence of reinforced particle fracture on strengthening of spray formed Cu-TiB2 composite. Scripta Materialia 39, 1063–1069. doi:10.1016/S1359-6462(98)00246-2
Lenoir, N., Bornert, M., Desrues, J., Bésuelle, P., Viggiani, G., 2007. Volumetric Digital Image Correlation Applied to X-ray Microtomography Images from Triaxial Compression Tests on Argillaceous Rock. Strain 43, 193–205. doi:10.1111/j.1475-1305.2007.00348.x
Liu, C.H., Nagel, S.R., Schecter, D.A., Coppersmith, S.N., Majumdar, S., Narayan, O., Witten, T.A., 1995. Force fluctuations in bead packs. Science 269, 513–515. doi:10.1126/science.269.5223.513
Lubachevsky, B.D., Stillinger, F.H., 1990. Geometric properties of random disk packings. Journal of Statistical Physics 60, 561–583. doi:10.1007/BF01025983
Mbiakop, A., Constantinescu, A., Danas, K., 2015. An analytical model for porous single crystals with ellipsoidal voids. Journal of the Mechanics and Physics of Solids 84, 436–

467. doi:10.1016/j.jmps.2015.07.011
McDowell, G.R., Harireche, O., 2002. Discrete element modelling of yielding and normal compression of sand. Géotechnique 52, 299–304. doi:10.1680/geot.52.4.299.41018
Pickering, E.G., Bele, E., Deshpande, V.S., 2016. Multi-axial response of idealized cermets. Acta Materialia 116, 281–289. doi:10.1016/j.actamat.2016.06.051
Powrie, W., Ni, Q., Harkness, R.M., Zhang, X., 2005. Numerical modelling of plane strain tests on sands using a particulate approach. Géotechnique 55, 297–306. doi:10.1680/geot.55.4.297.65492
Shockey, D., Marchand, A., Skaggs, S., Cort, G., Burkett, M., Parker, R., 1990. Failure phenomenology of confined ceramic targets and impacting rods. International Journal of Impact Engineering 9, 263–275. doi:10.1016/0734-743X(90)90002-D
Tarantino, M.G., Weber, L., Mortensen, A., 2016. Effect of hydrostatic pressure on flow and deformation in highly reinforced particulate composites. Acta Materialia 117, 345–355. doi:10.1016/j.actamat.2016.06.052
Taya, M., Lulay, K.E., Lloyd, D.J., 1991. Strengthening of a particulate metal matrix composite by quenching. Acta Metallurgica et Materialia 39, 73–87. doi:10.1016/0956-7151(91)90329-Y
Tinklepaugh, J.R., Crandall, W.B., 1960. Cermets. Reinhold Publishing Company, New York.
Travers, T., Ammi, M., Bideau, D., Gervois, A., Messager, J., Troadec, J., 1987. Uniaxial Compression of 2d Packings of Cylinders. Effects of Weak Disorder . Europhysics Letters 4, 329–332. doi:10.1209/0295-5075/4/3/012
Walley, S.M., 2010. Historical review of high strain rate and shock properties of ceramics relevant to their application in armour. Advances in Applied Ceramics 109, 446–466. doi:10.1179/174367609X422180
Wu, J., Collop, A.C., McDowell, G.R., 2011. Discrete Element Modeling of Constant Strain Rate Compression Tests on Idealized Asphalt Mixture. Journal of Materials in Civil Engineering 23, 2–11. doi:10.1061/(ASCE)MT.1943-5533.0000002